Haftkoeffizienten und Adsorptionskinetik

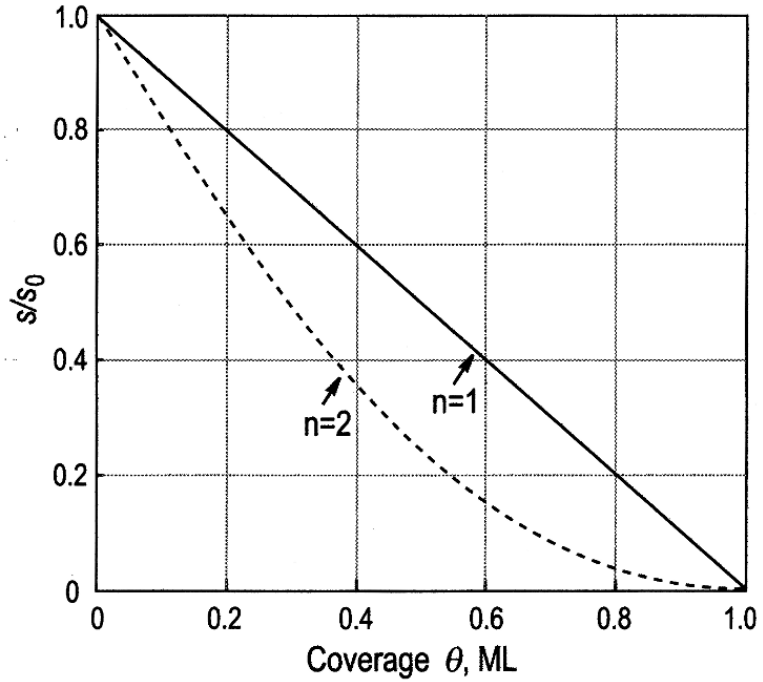

Langmuir adsorption

Sticking coefficient

$$s = s_0(1 - \Theta)^n$$

$n = 1$ – non-dissociative,
$n = 2$ – dissociative.

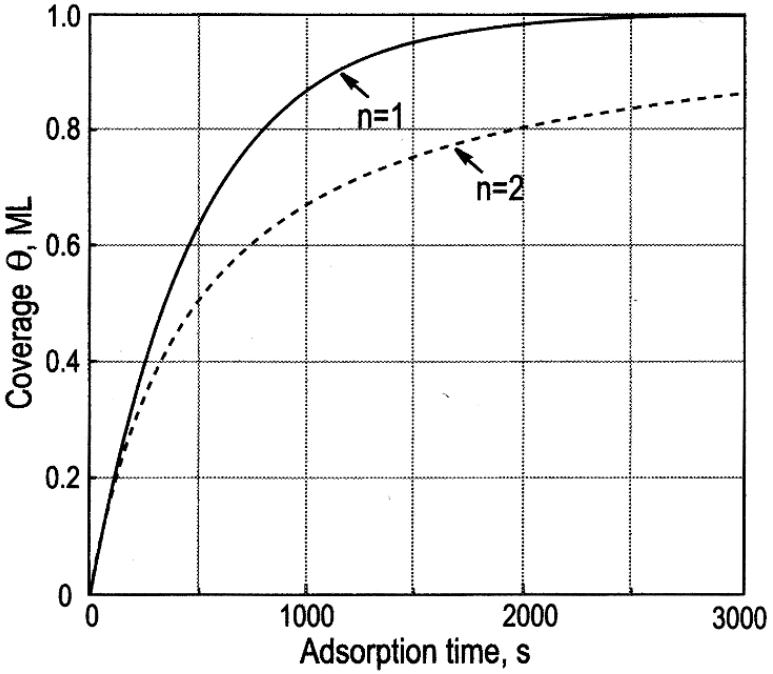

Adsorption kinetics

non-dissociative ($n = 1$):

$$\Theta = 1 - \exp(-s_0 I \cdot t)$$

dissociative ($n = 2$):

$$\Theta = \frac{s_0 I \cdot t}{1 + s_0 I \cdot t}$$

Fig. 12.1. Sticking coefficient and adsorption kinetics for non-dissociative first-order ($n = 1$) and dissociative second-order ($n = 2$) Langmuir adsorption. The kinetic curves are calculated for an adsorbate flux of 0.002 ML/s.

Haftkoeffizient von O_2 auf Rh bei 110 K

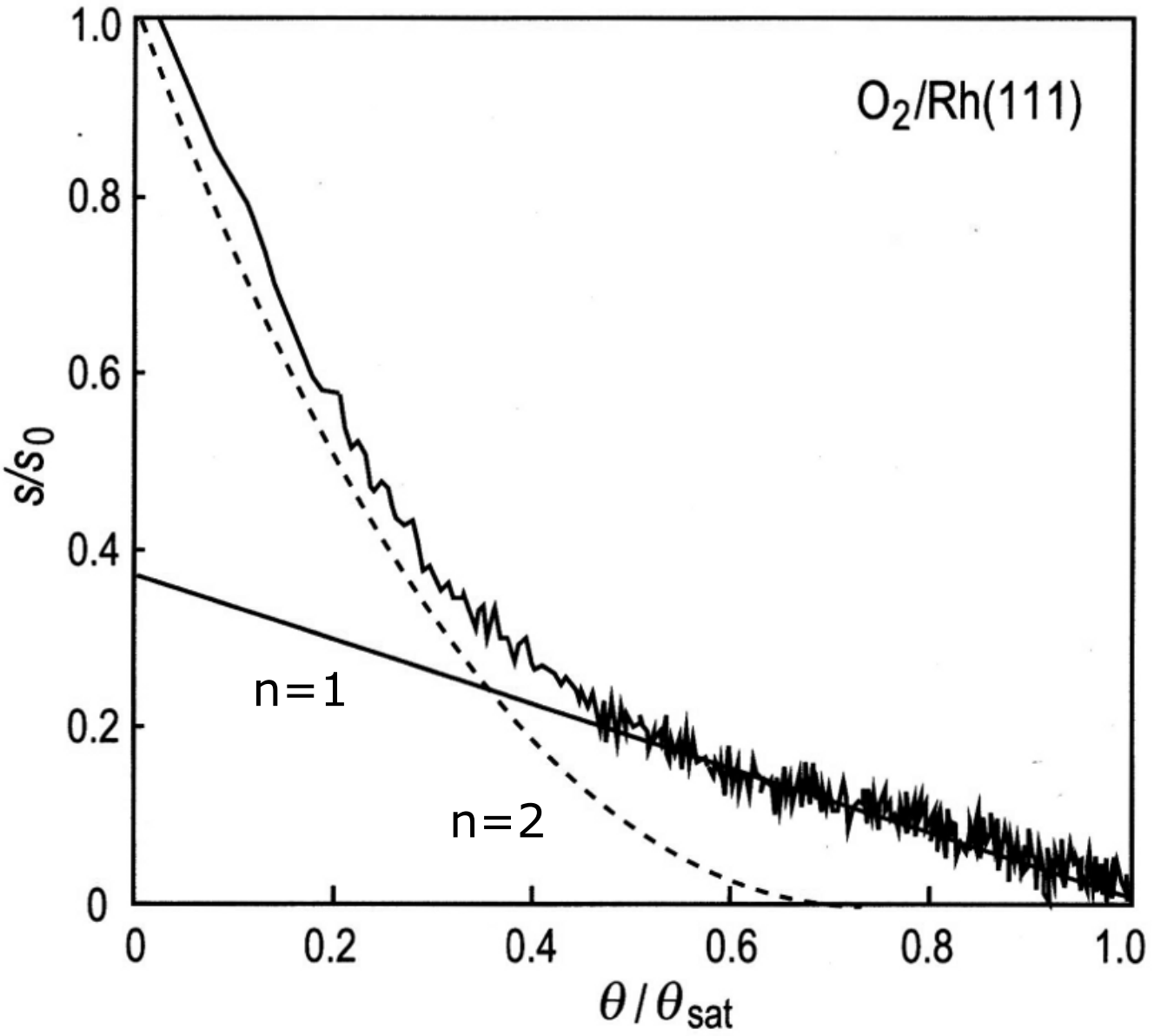

Fig. 12.2. Time evolution of the sticking coefficient of O_2 on Rh(111). The incident beam energy is 490 meV, and the substrate temperature is 110 K. The dashed and solid lines are the fits using, respectively, first- and second-order Langmuir kinetics (after Brault et al. [12.1])

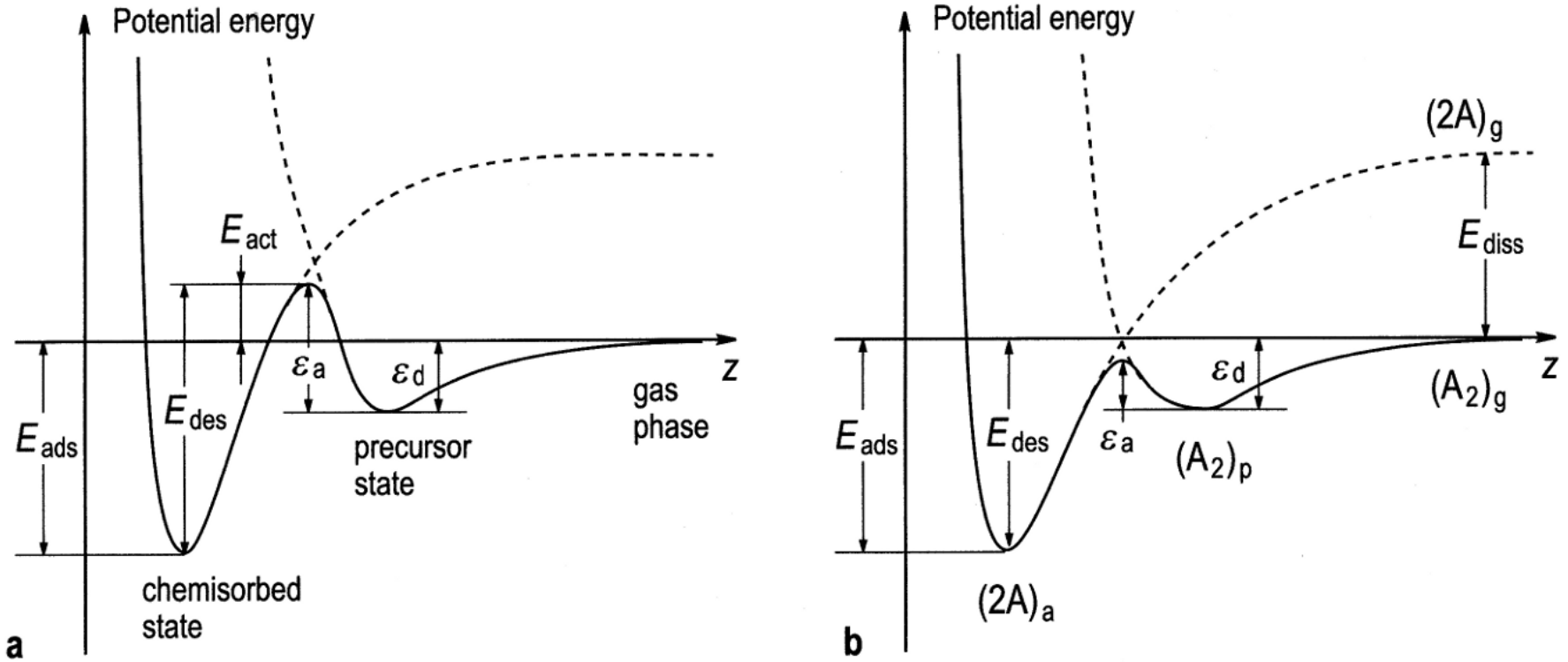

Fig. 12.8. Schematic of the potential energy curves for precursor-mediated chemisorption: (**a**) the case of activated chemisorption with an activation barrier of $E_{act} = \varepsilon_a - \varepsilon_d$; (**b**) the case of non-activated chemisorption with $\varepsilon_a < \varepsilon_d$. The pathway for precursor-mediated dissociative adsorption, $(A_2)_g \rightarrow (A_2)_p \rightarrow (2A)_a$ is shown in (**b**). E_{ads} is the binding energy in the chemisorbed state, E_{des} the barrier for desorption from the chemisorbed state, ε_a and ε_d denote respectively the barriers for adsorption and desorption from the precursor state well, $E_{act} = \varepsilon_a - \epsilon_d$ is the activation barrier for chemisorption, and E_{diss} is the dissociation energy of the molecule in the gas phase

Haftkoeffizienten bei Precursor

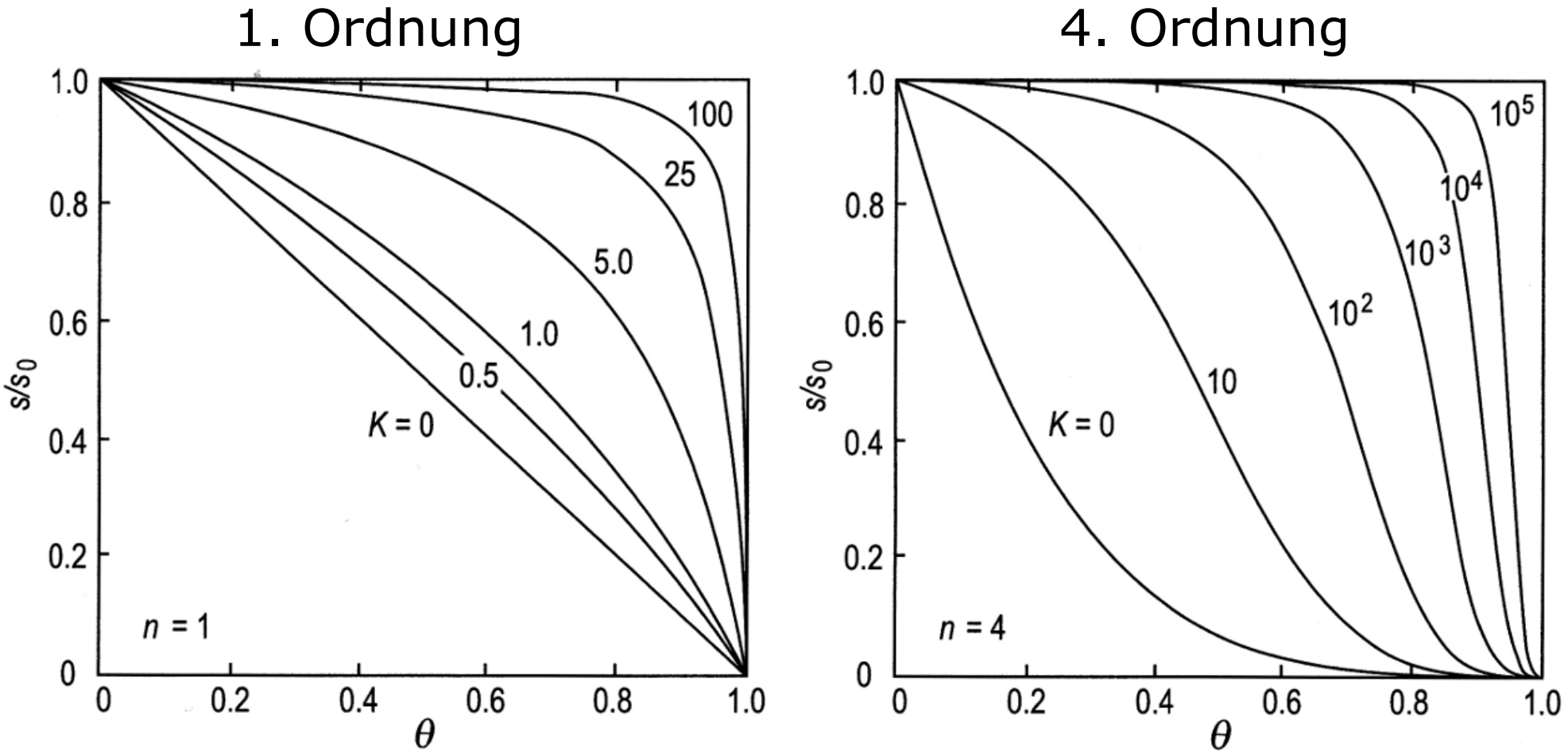

Fig. 12.3. Coverage dependent sticking probability for precursor-mediated chemisorption of non-interacting adsorbates as calculated using (12.12) (**a**) for first-order kinetics ($n = 1$) and (**b**) for fourth-order kinetics ($n = 4$). The precursor parameter is $K = k_a/k_d$ (after Lombardo and Bell [12.2])

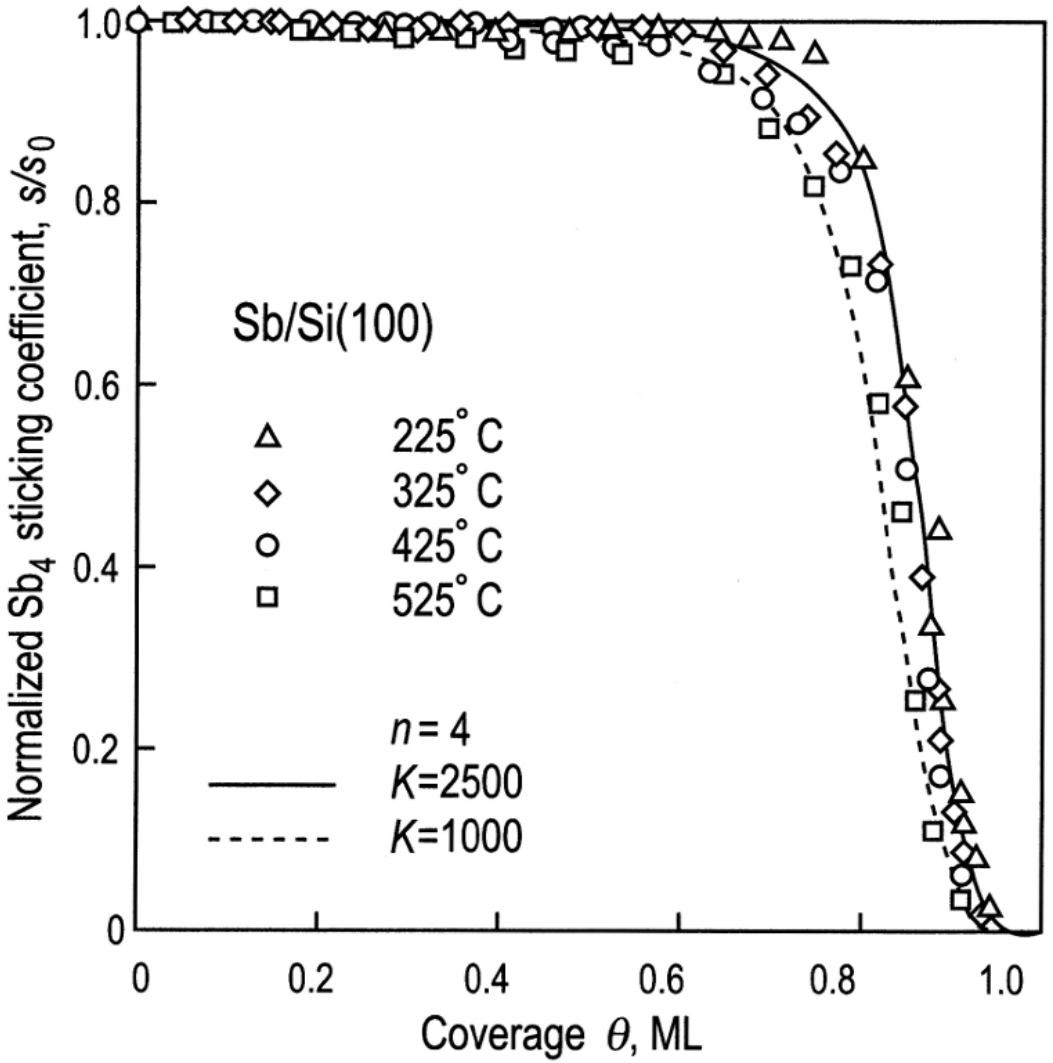

Fig. 12.4. Coverage dependence of the sticking coefficient of Sb on Si(100). The curves are calculated from (12.12) for $n = 4$ and $K = 2500$ (solid line) and $K = 1000$ (dashed line) (after Barnett et al. [12.3])

Fig. 12.12. Ideal time dependence of adsorbate surface coverage calculated for zero-, first-, and second-order desorption kinetics and various temperatures. All rate constants k_n are assumed to be 10^{13}, the activation energy for desorption is $E_{\mathrm{des}} = 3\,\mathrm{eV}$, and $\Theta_0 = 1\,\mathrm{ML}$.

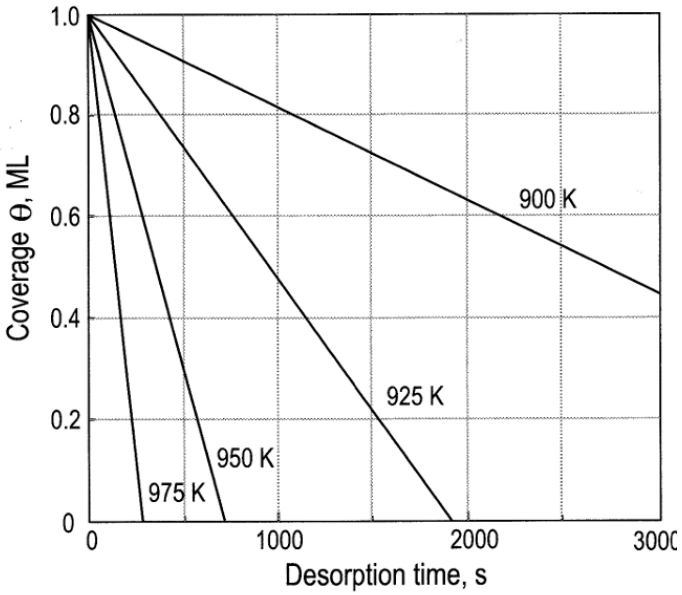

Zero-order $(n = 0)$

$$\Theta = \Theta_0 \left(1 - \frac{k_0 \cdot t}{\Theta_0}\right),$$

where

$$k_0 = k_0^0 \exp\left(\frac{-E_{\mathrm{des}}}{k_{\mathrm{B}} T}\right),$$

$$[k_0] = \left[\frac{\mathrm{ML}}{\mathrm{s}}\right].$$

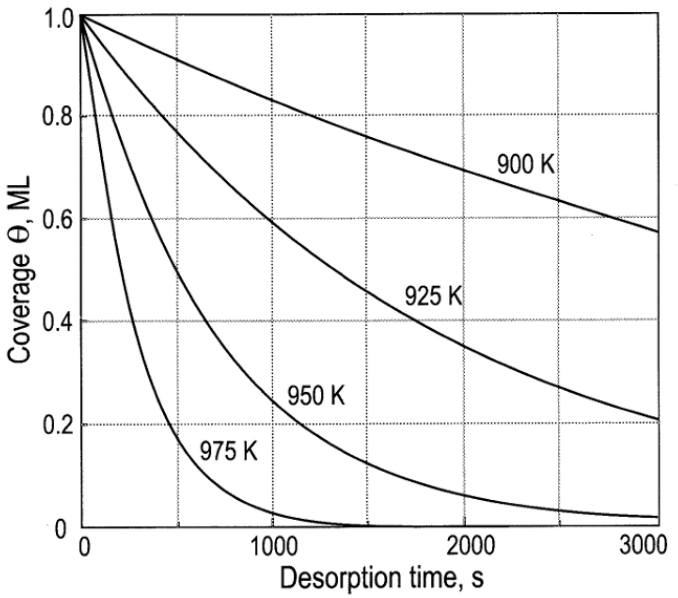

First-order $(n = 1)$

$$\Theta = \Theta_0 \exp(-k_1 \cdot t),$$

where

$$k_1 = k_1^0 \exp\left(\frac{-E_{\mathrm{des}}}{k_{\mathrm{B}} T}\right),$$

$$[k_1] = \left[\frac{1}{\mathrm{s}}\right].$$

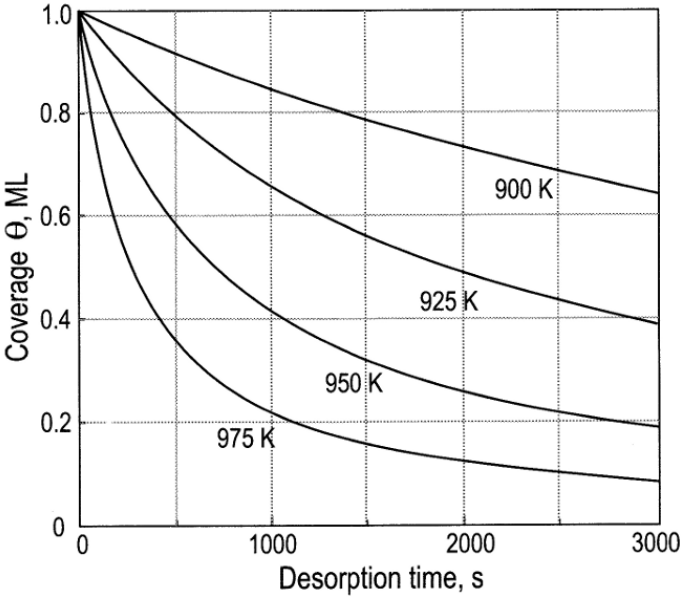

Second-order $(n = 2)$

$$\Theta = \frac{\Theta_0}{1 + k_2 \Theta_0 \cdot t},$$

where

$$k_2 = k_2^0 \exp\left(\frac{-E_{\mathrm{des}}}{k_{\mathrm{B}} T}\right)$$

$$[k_2] = \left[\frac{1}{\mathrm{ML} \cdot \mathrm{s}}\right].$$

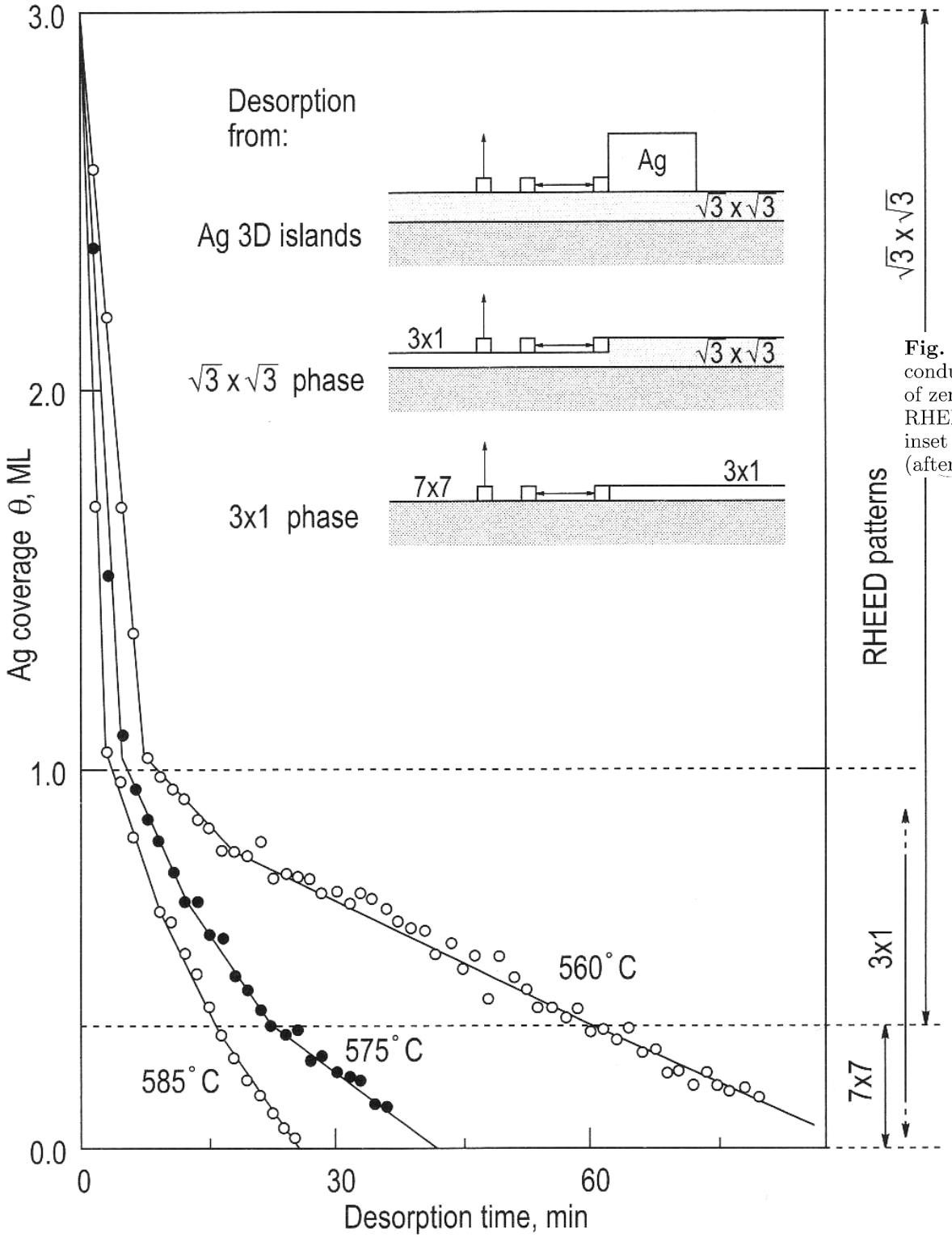

Fig. 12.15. Variation of the Ag coverage on Si(111) during isothermal desorption conducted at 560°C, 575°C, and 585°C. The desorption is represented as a set of zero-order kinetics with rate constants depending on the surface structure. The RHEED patterns that are observed simultaneously are shown in the right panel. The inset illustrates the desorption mechanism which accounts for zero-order kinetics (after Hasegawa et al. [12.9])

Ordnung n

n = 0 n = 1 n = 2

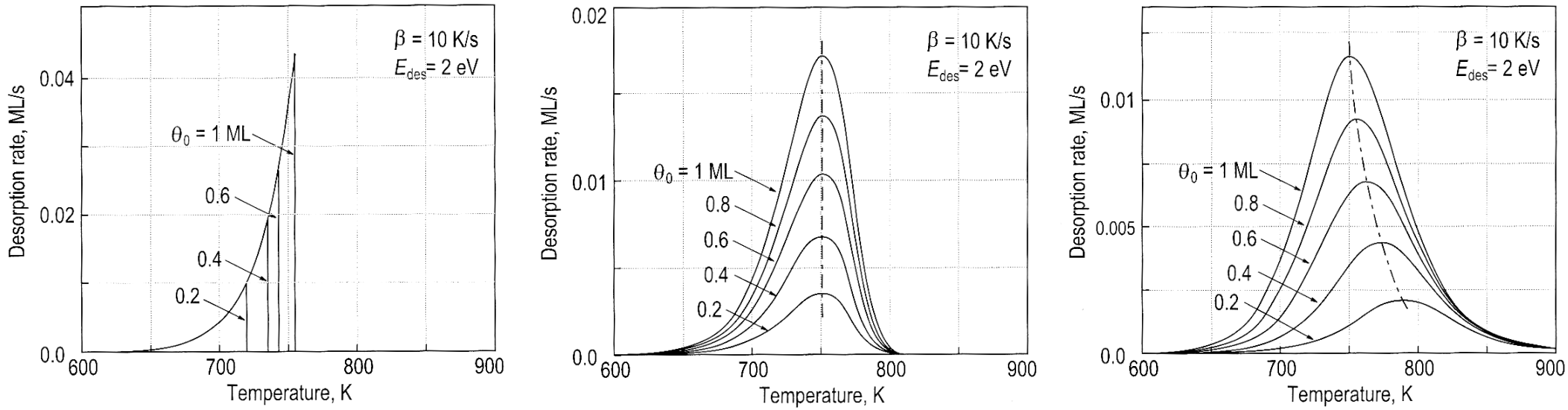

Fig. 12.18. TPD spectra calculated for zero-order, first-order, and second-order desorption kinetics and various initial coverages Θ_0. Both the pre-exponential factor and activation energy for desorption are assumed to be independent of the surface coverage Θ. The heating rate is assumed to be linear and of magnitude β. Note the different scales for different desorption orders. Only the integrated area under the peaks is proportional to the initial coverage Θ_0

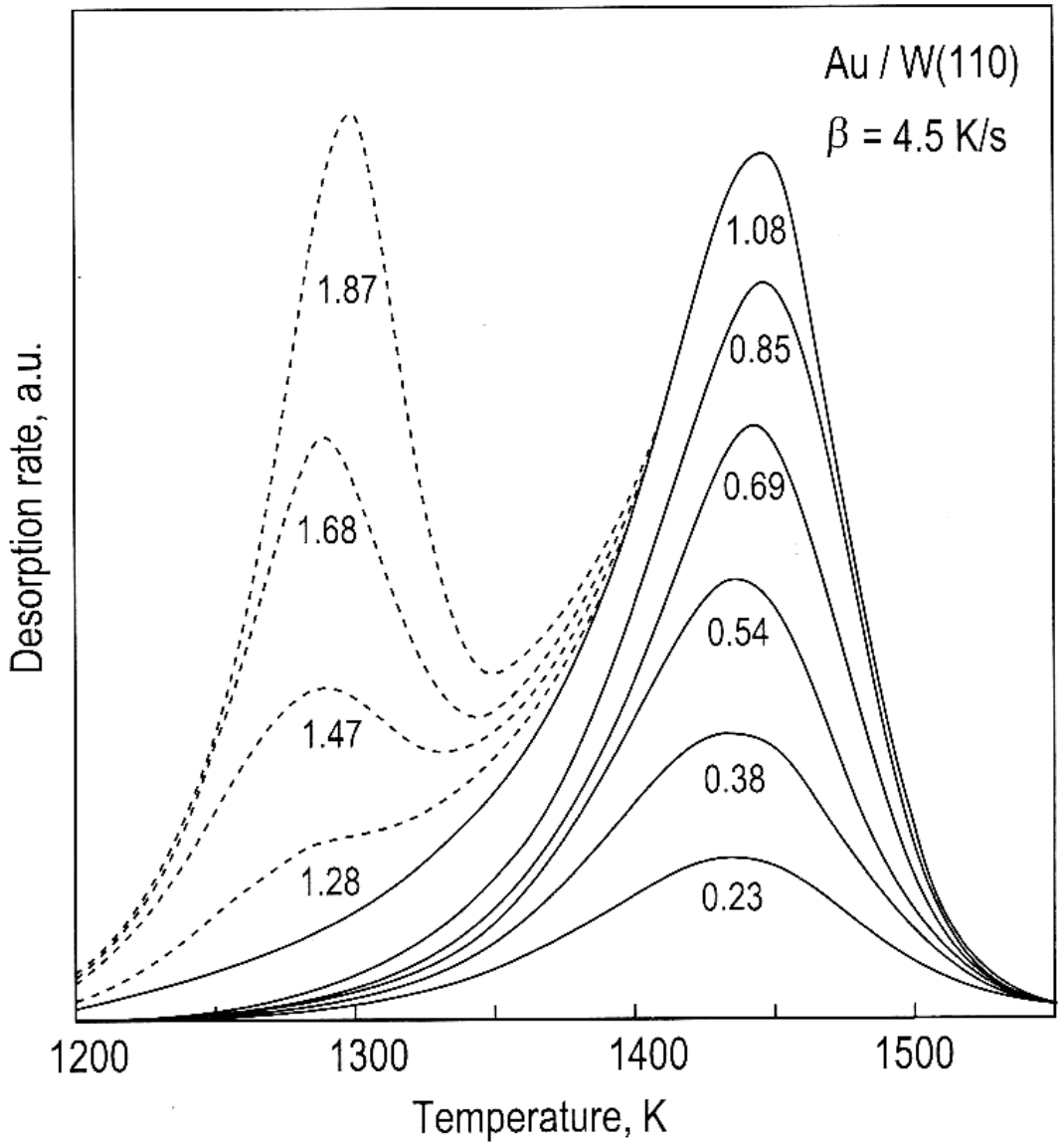

Fig. 12.19. TPD spectra of Au from W(110). The high-temperature peak (solid line) is due to the first Au monolayer, the low-temperature peak (dashed line) is due to the second Au monolayer. Parameters indicate the initial Au coverage in monolayers (after Bauer et al. [12.11])

Diffusion: Aktivierungsenergie

Übergangszustand

Adsorptionsplatz

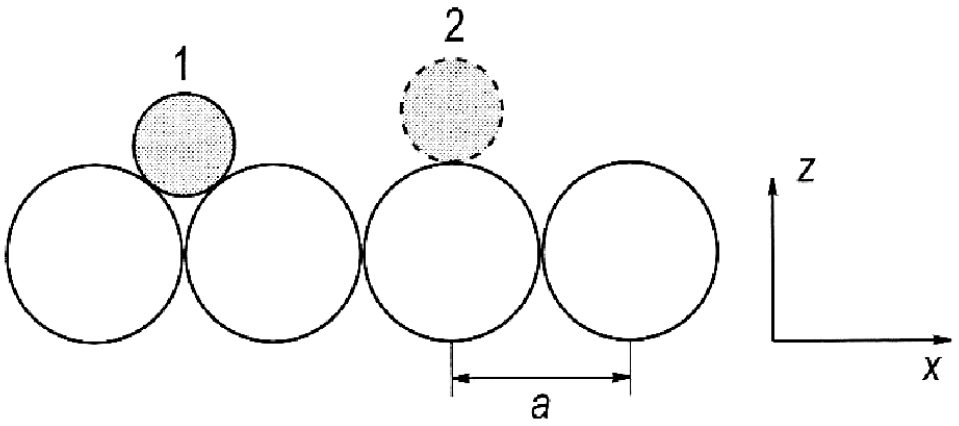

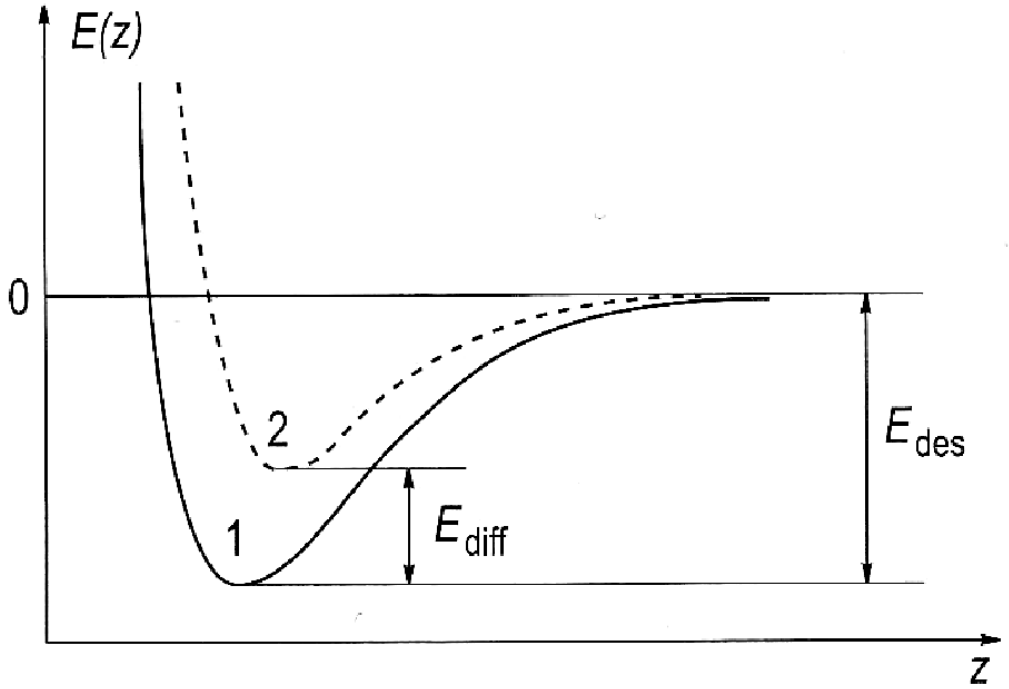

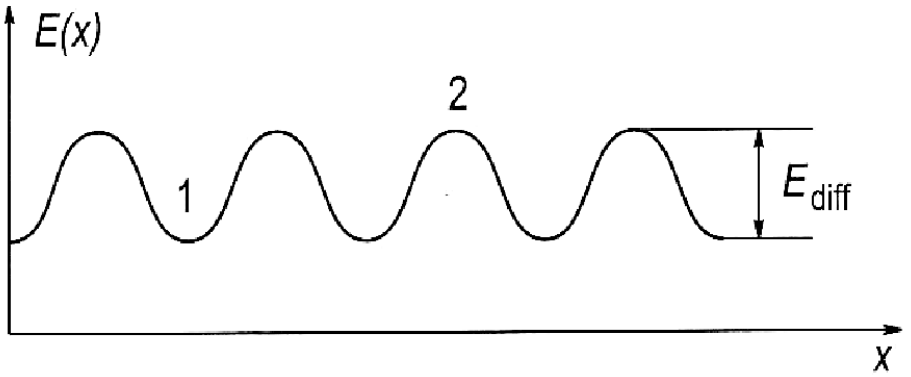

Rechnungen für diverse Diffusionslängen $2(Dt)^{1/2}$

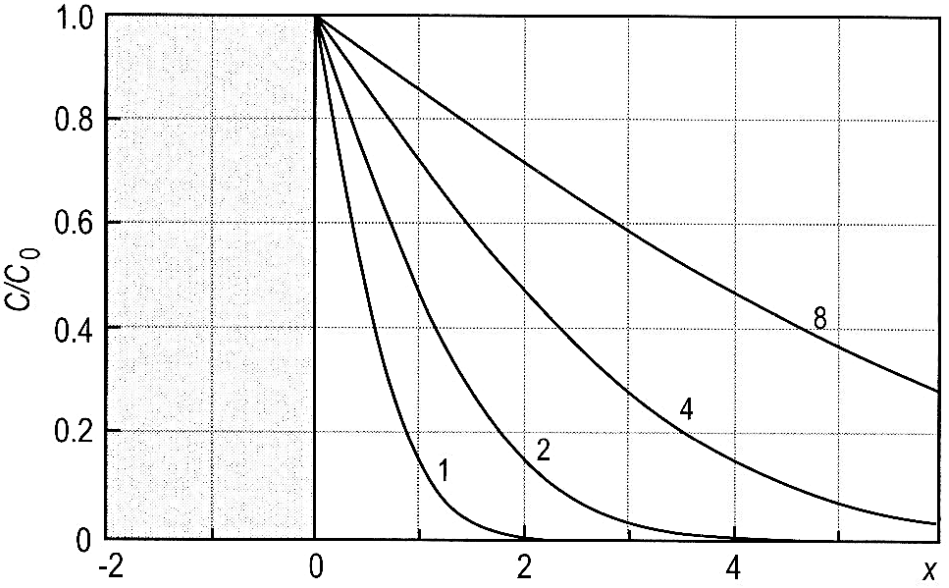

Bereich fester Konzentration c_0

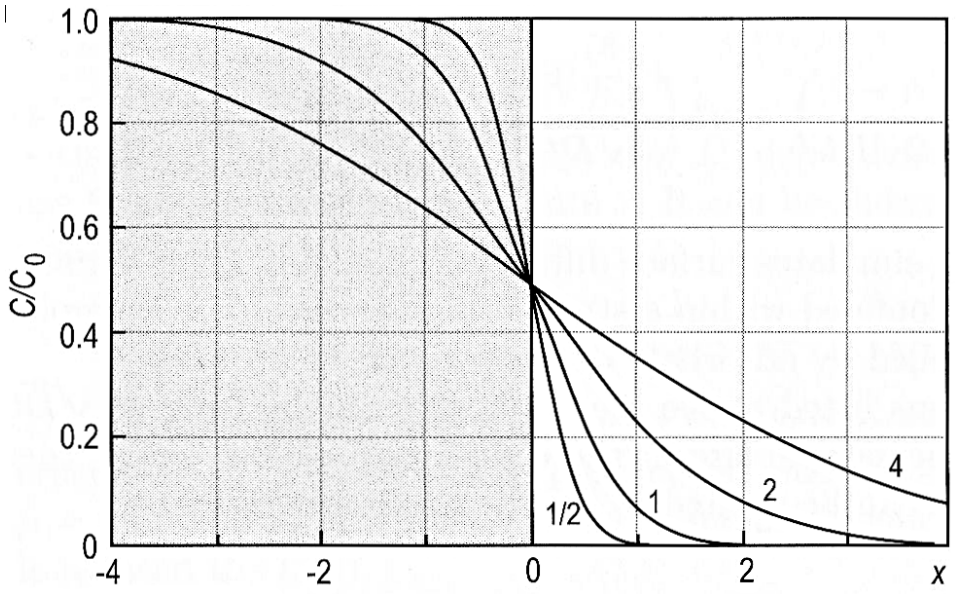

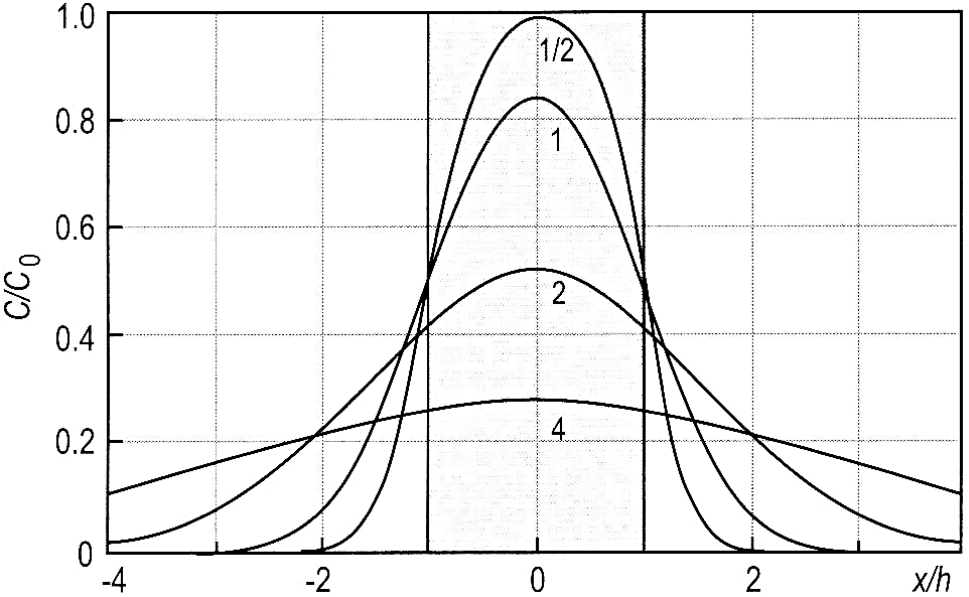

Anfänglich: Stufe c_0 - 0

Linie 0 - c_0 - 0

Diffusion von Rhodiumadatomen auf Rhodium: Einfluss der Oberflächenorientierung

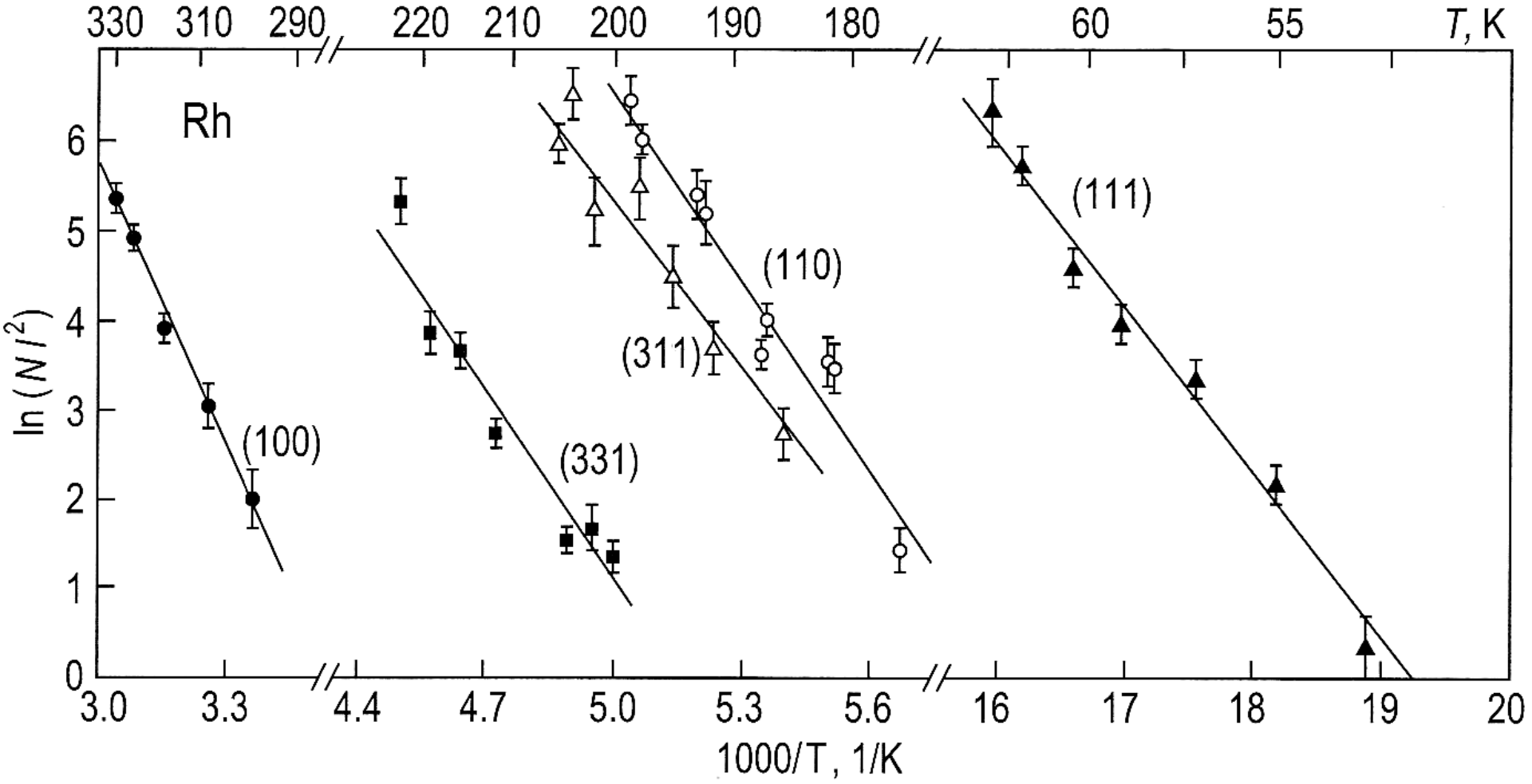

N: Zahl der Sprünge in 3 min, l Sprungweite

* auf (110), (311), (331): 1d Diffusion längs [110]; senkrecht dazu nicht messbar

* auf (111), (100): isotrop

Diffusion von Ni auf W(110): Einfluss von Stufen

T = 1170 K

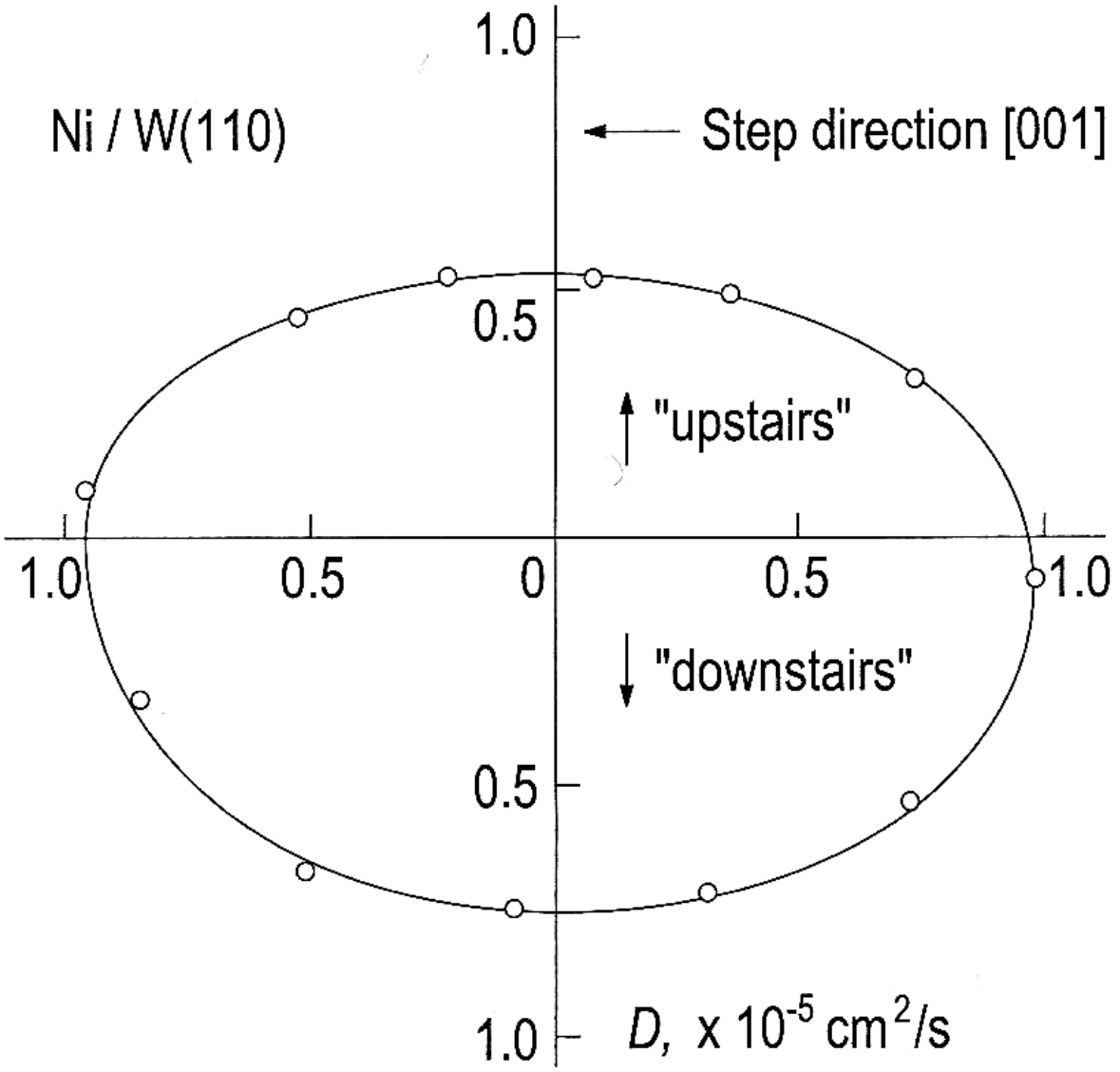

''Einfaches'' Hüpfen: N auf Fe(100)

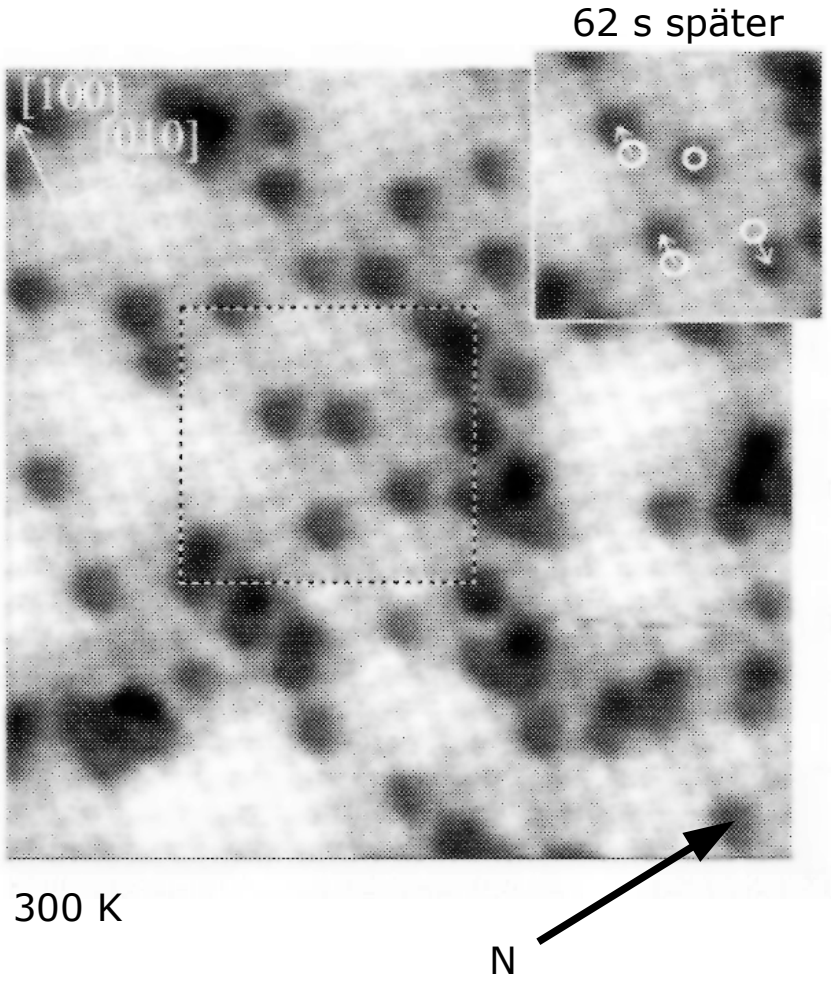

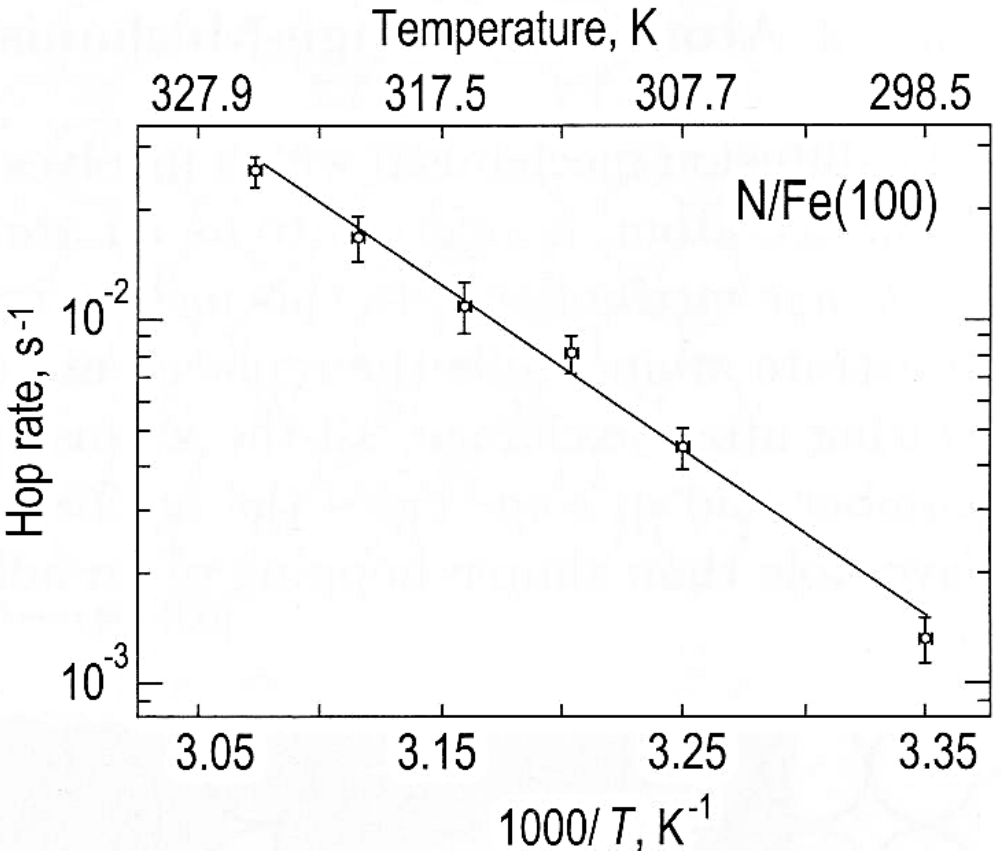

E_{diff} = 0.92 +/- 0.04 eV

v_0 = 4.3 x 10^{12} s^{-1}

Einfach ?

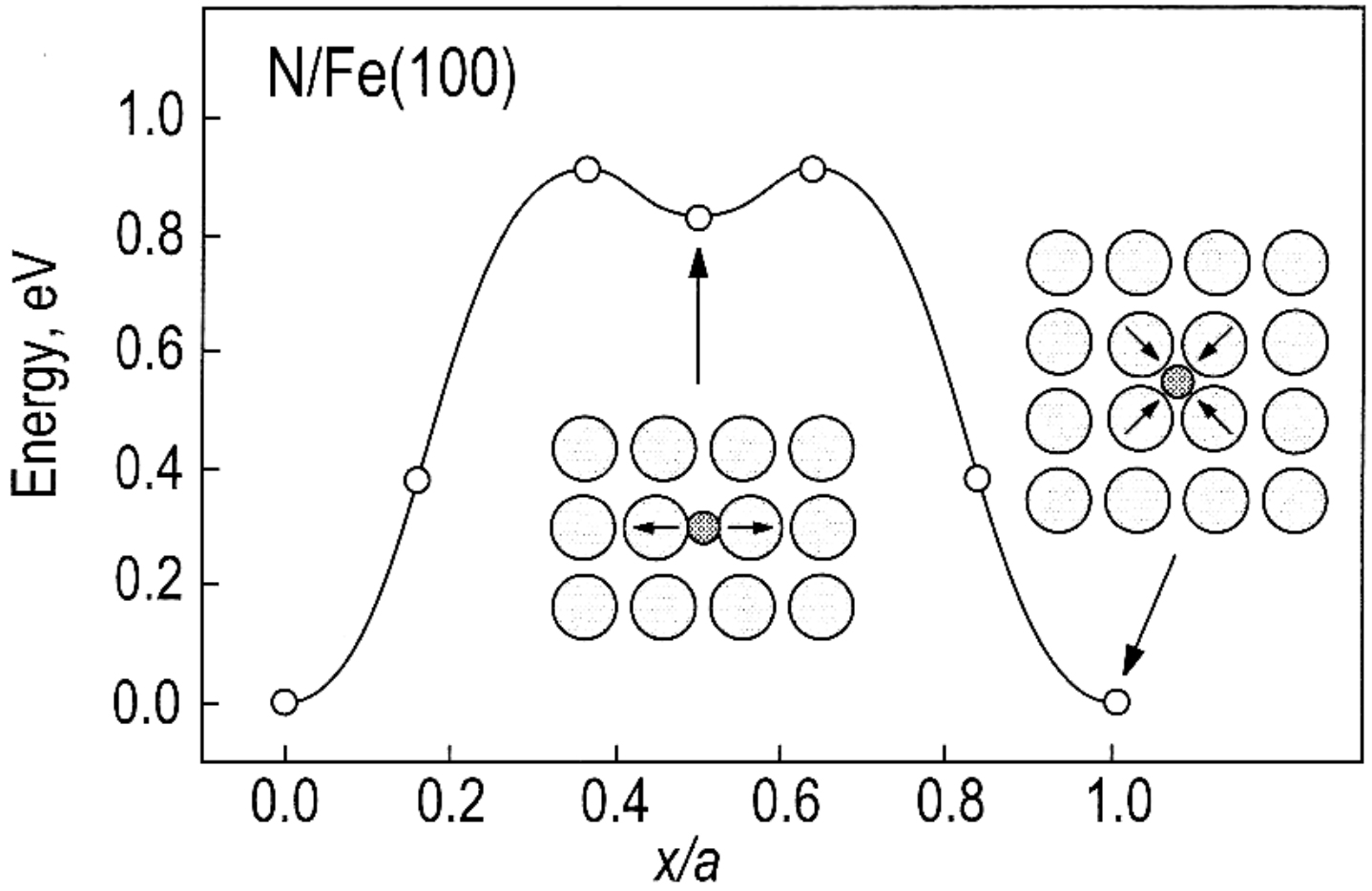

Fig. 13.10. Hopping diffusion of nitrogen adatoms on Fe(100): Calculated shape of the potential barrier between the two neighboring fourfold hollow adsorption sites. The energy of the maximum is 0.91 eV with a shallow metastable minimum at 0.83 eV. The insets illustrate the distortion in the Fe(100) top layer (indicated by arrows) induced by the nitrogen adatom in the stable fourfold hollow site and in the metastable bridge site (after Pedersen et al. [13.7])

Low-temperature manipulation of Ag atoms & clusters on Ag(110)
Appl. Phys. A 66, S675 (1998)

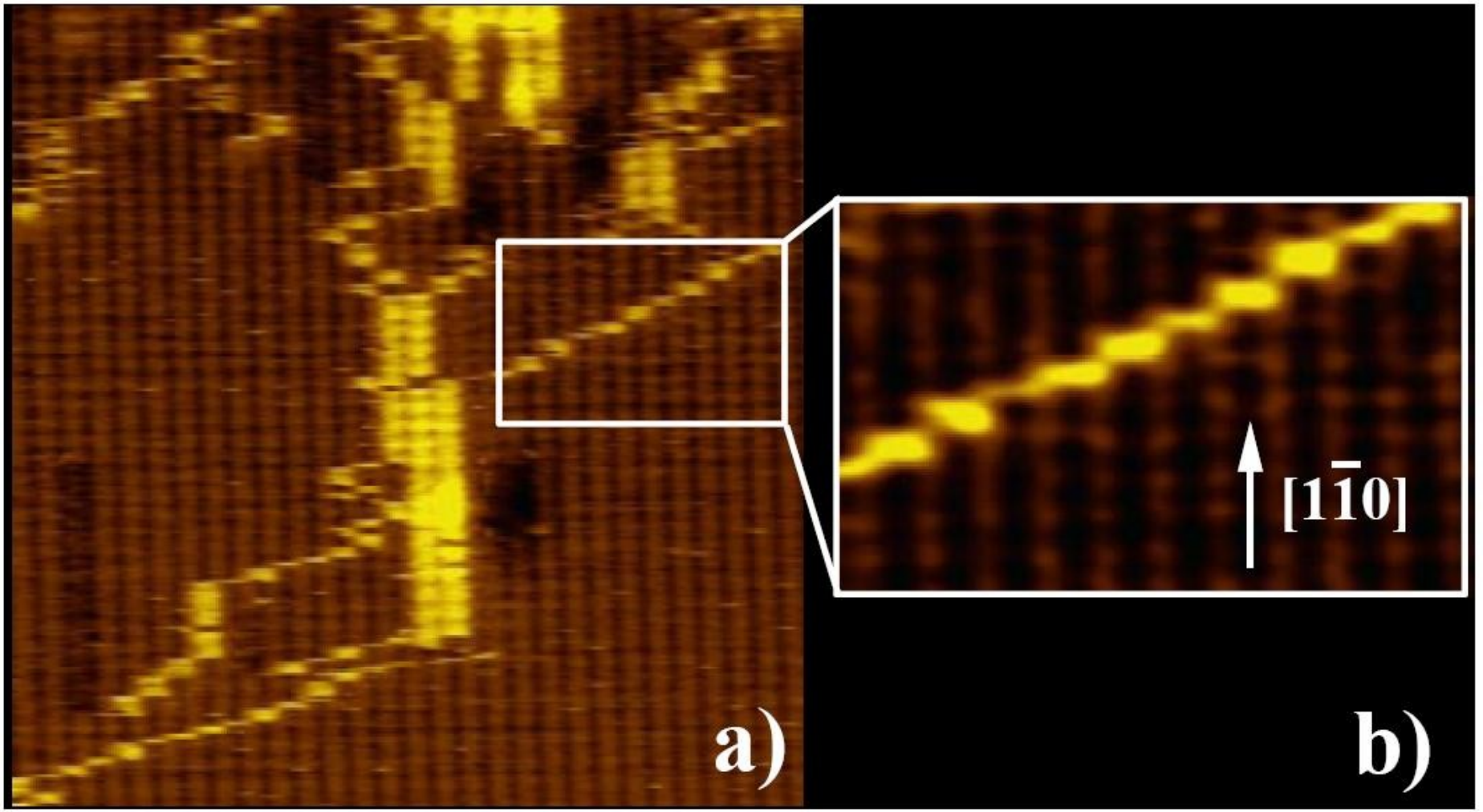

Fig. 4a,b. SMM of Ag clusters and adatoms on Ag(110) at $V = 0.27$ V, $I = 58$ nA. **a** clusters and single atoms, **b** enlarged view of diagonal [1$\bar{1}$1] Ag adatom motion

H-Diffusion

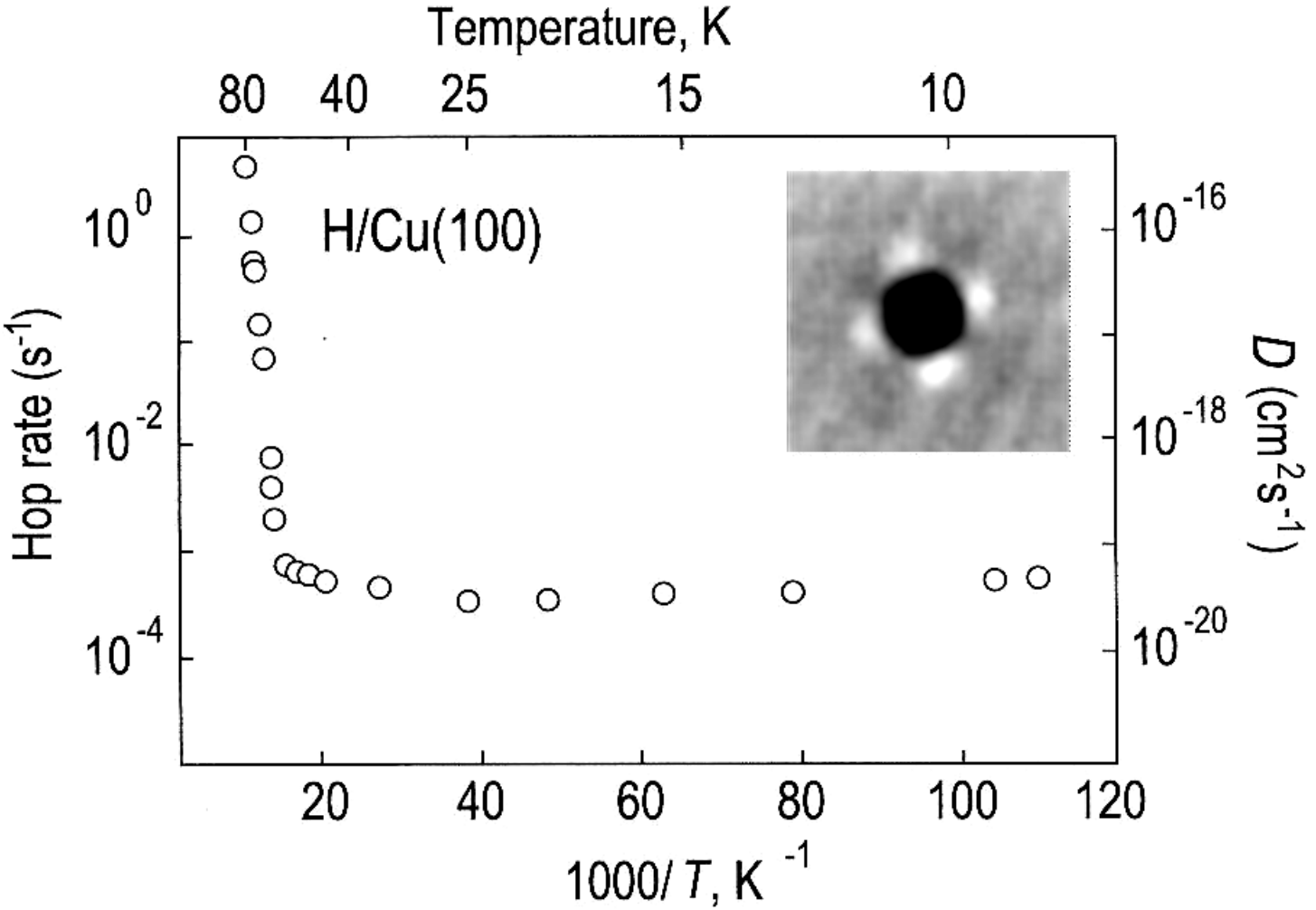

Fig. 13.13. Classical and quantum diffusion of H on Cu(100): Arrhenius plot of the hopping rate of the individual H atoms between 80 and 9 K. The right axis gives the equivalent single particle diffusion coefficient, D, which is related to the hop frequency ν by the expression $D = a^2\nu/4$, where the lattice constant is $a = 2.55$ Å. The inset shows a 15×15 Å^2 STM image of an isolated H atom on Cu(100) (after Lauhon and Ho [13.10])

Diffusion über Stufen: Ehrlich-Schwoebel-Barriere

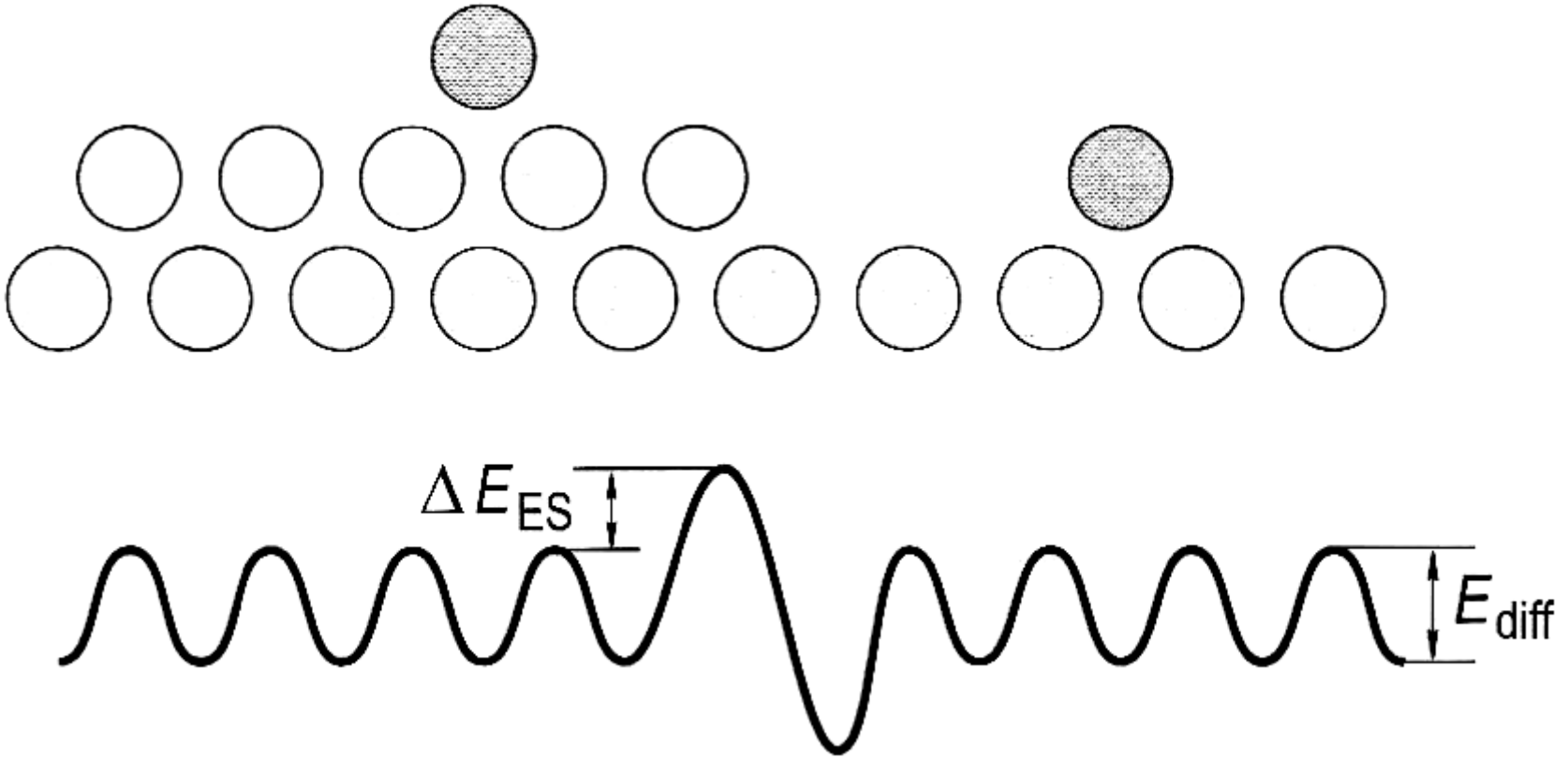

Fig. 14.21. Schematic representation of the potential energy variations associated with a monatomic step. E_{ES} denotes the Ehrlich–Schwoebel barrier, which an adatom (dark circle) has to surmount in addition to the terrace diffusion barrier E_{diff} in order to cross the step edge in the downward direction (after Schwoebel and Shipsey [14.14])

Diffusion über Stufen: mögliche atomare Prozesse

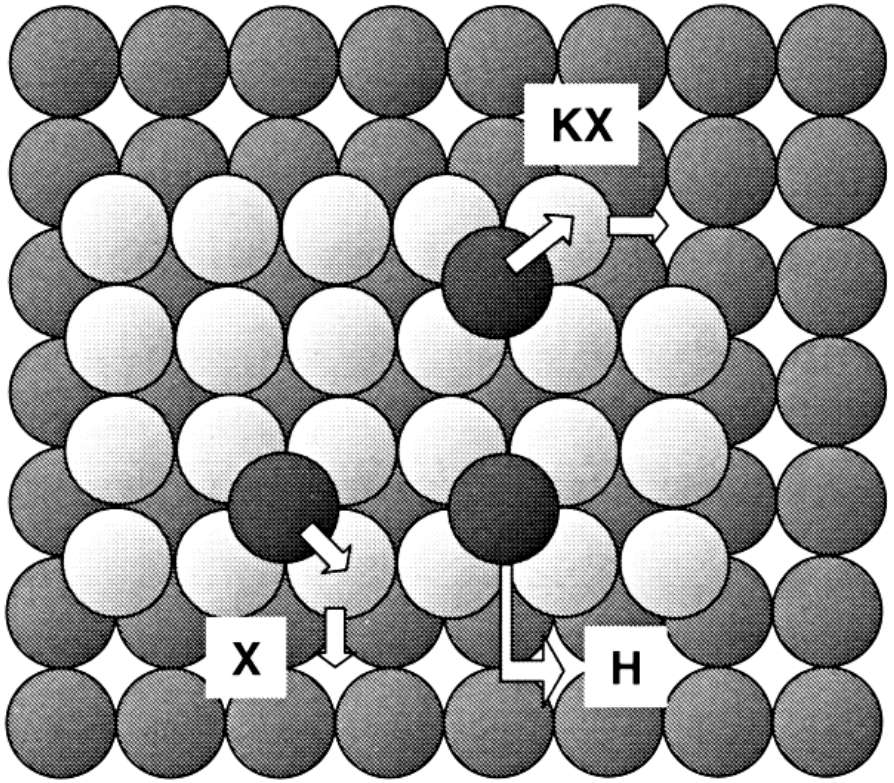

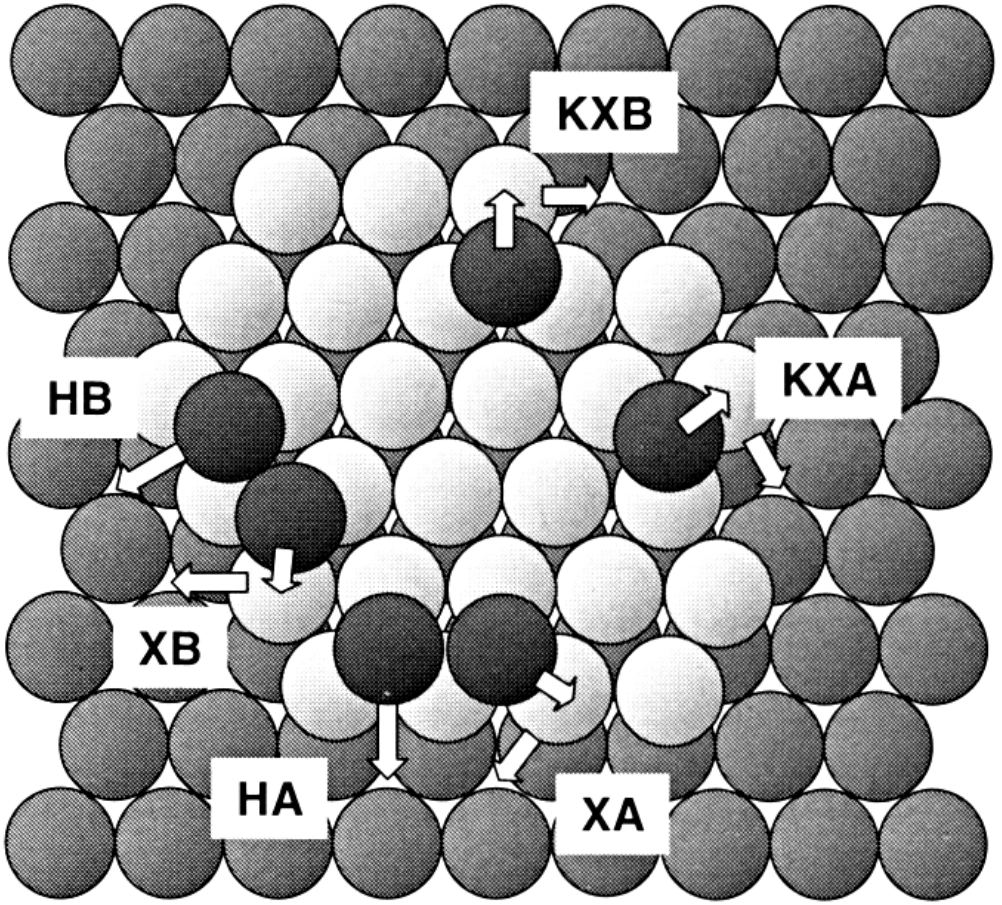

Hopping e**X**change **K**ink site **A** or **B** step

Calculated energies:

Table 10.3. ES-barriers in eV for hopping "H", for exchange "X", and exchange at kink sites "KX" for steps on some fcc(100) surfaces and of the A- and B-steps on Ag(111) and Pt(111). TH and TV denote the activation energies for hopping diffusion of adatoms and vacancies, respectively, and SV and KV the activation barriers for the filling of a vacancy next to a step by atoms from a straight step and a kink site.

	Cu(100)	Ag(100)	Ni(100)		Ag(111)	Pt(111)	Pt(111)
H	0.179	0.114	0.289	HA	0.44		0.24
X	0.232	0.149	0.113	AB	0.43		0.49
KX	-0.021	-0.044	-0.160	XA	0.31	0.22	0.02
TH	0.399	0.367	0.631	XB	0.06	0.10	0.35
TV	0.482	0.412	0.655	KXA	0.19		
SV	0.166	0.170	0.178	KXB	0.05		
KV	0.143	0.198	0.230				

Clusterdiffusion: Pt auf Pt(111)

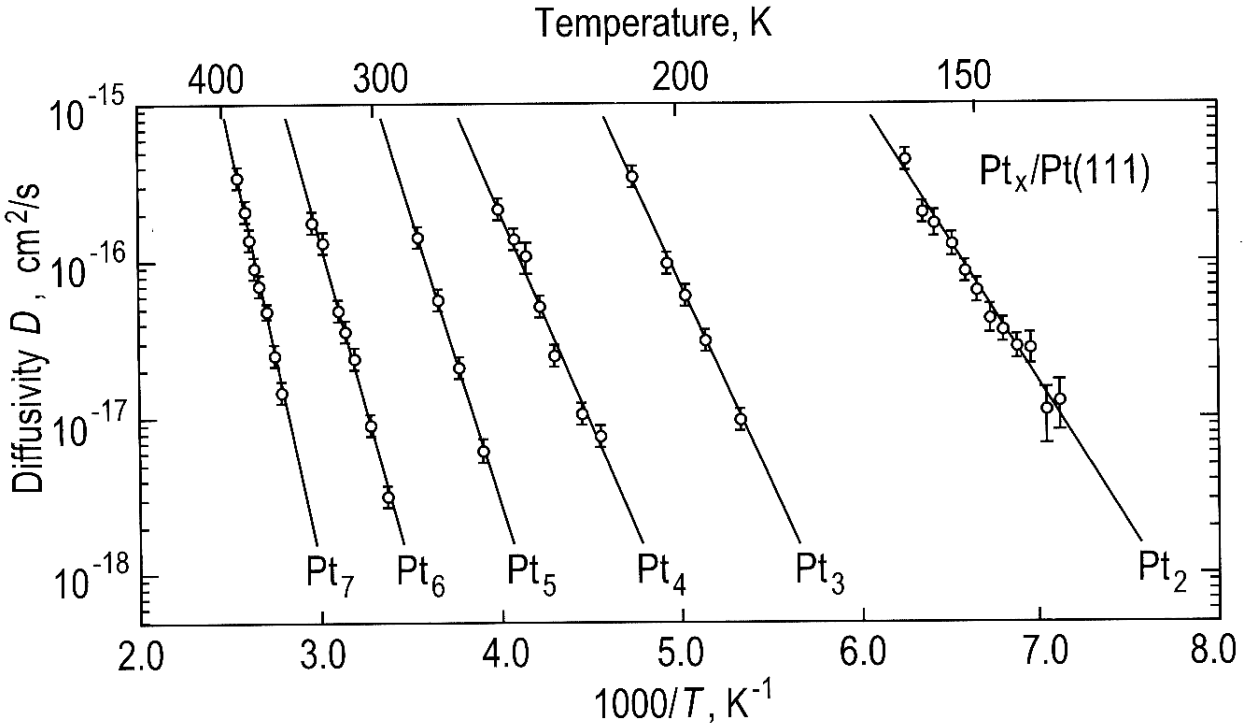

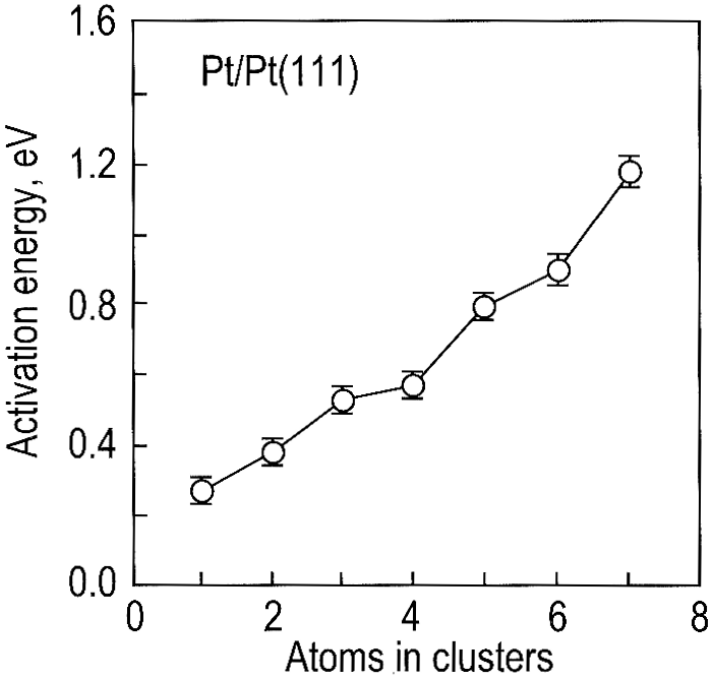

größer: langsamer

Clusterdiffusion: Elementarschritte

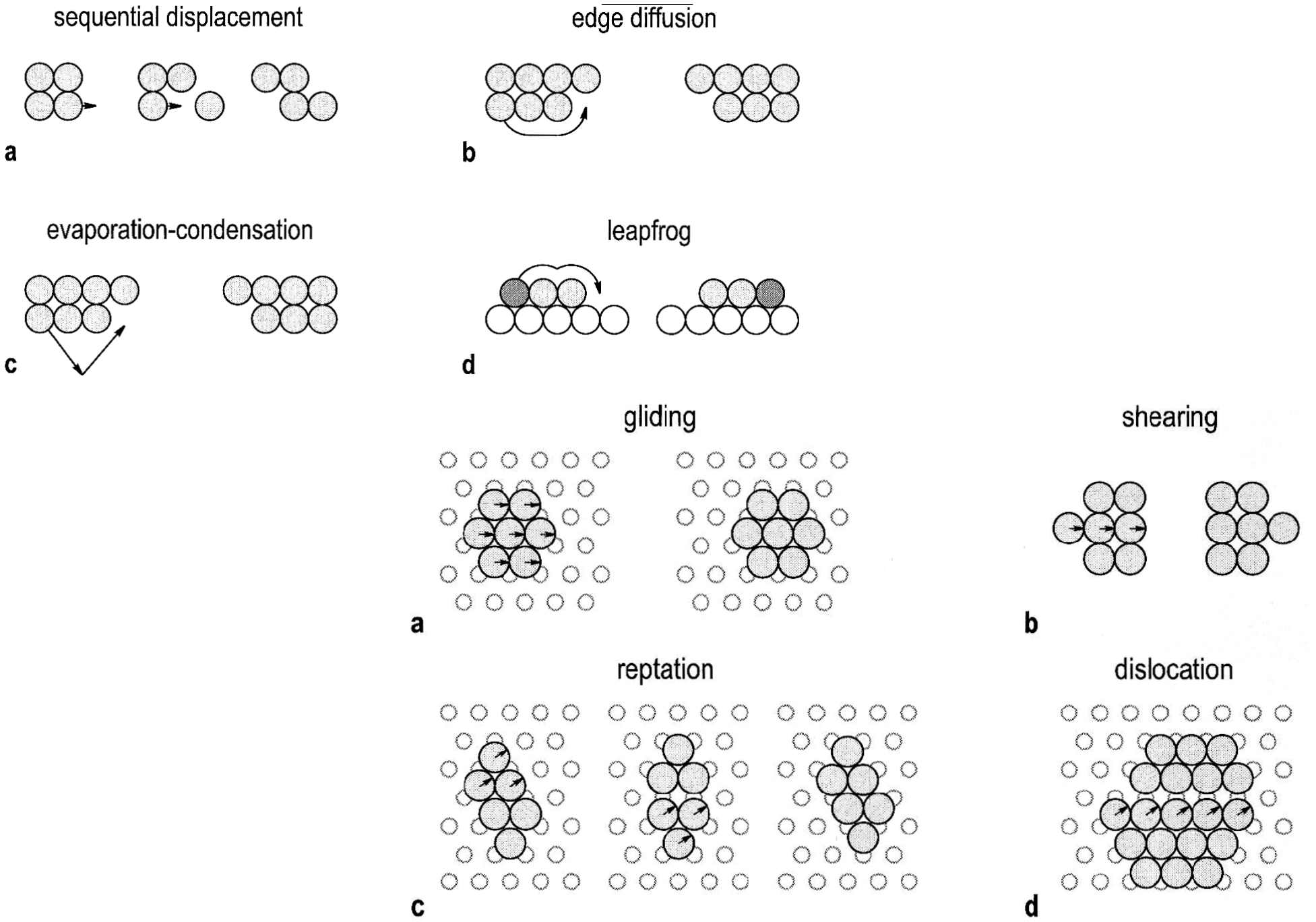

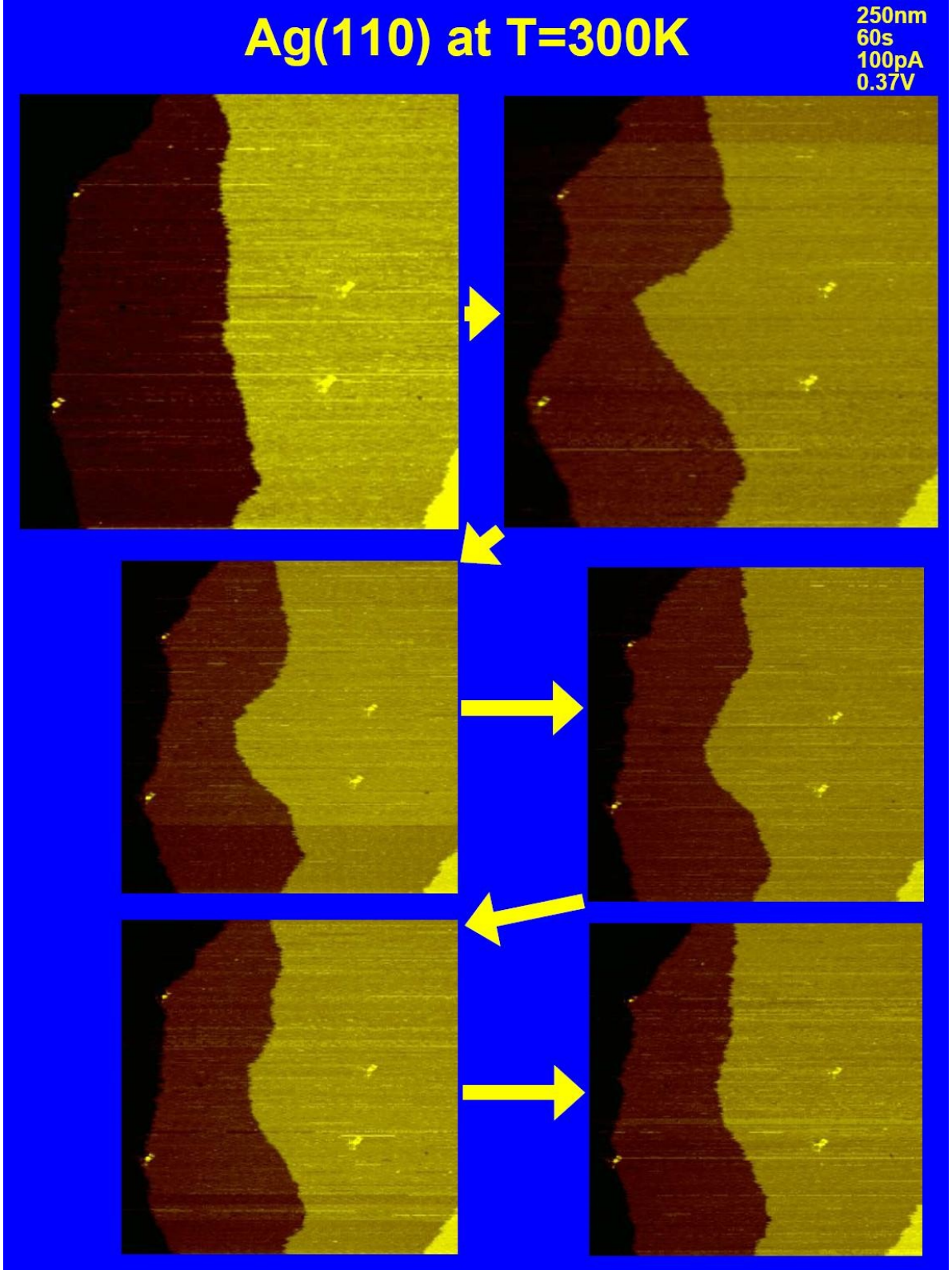
Ag(110) at T=300K
250nm
60s
100pA
0.37V

Wachstumsmodi

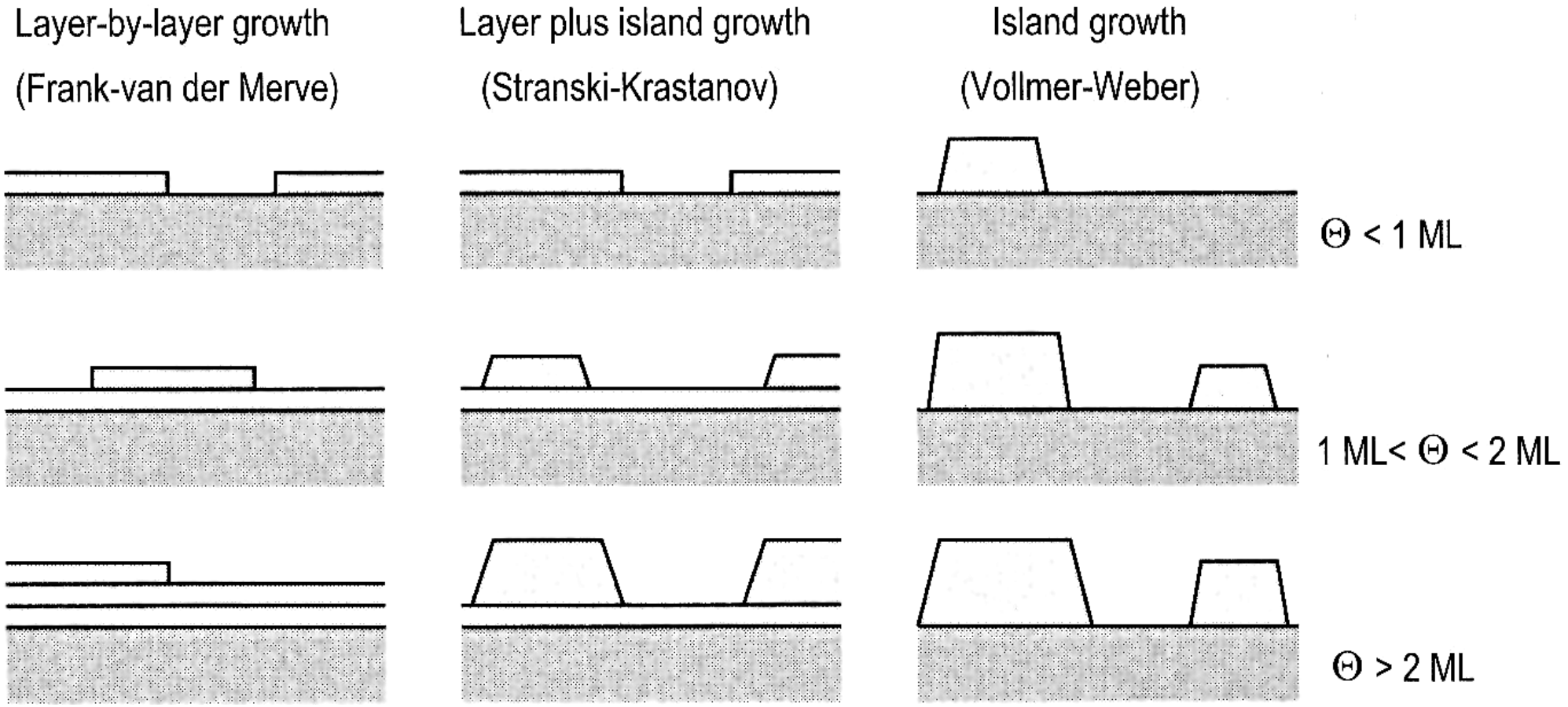

Surface tensions

vacuum-substrate γ_S

vacuum-film γ_F

interface film-substrate $\gamma_{F/S}$

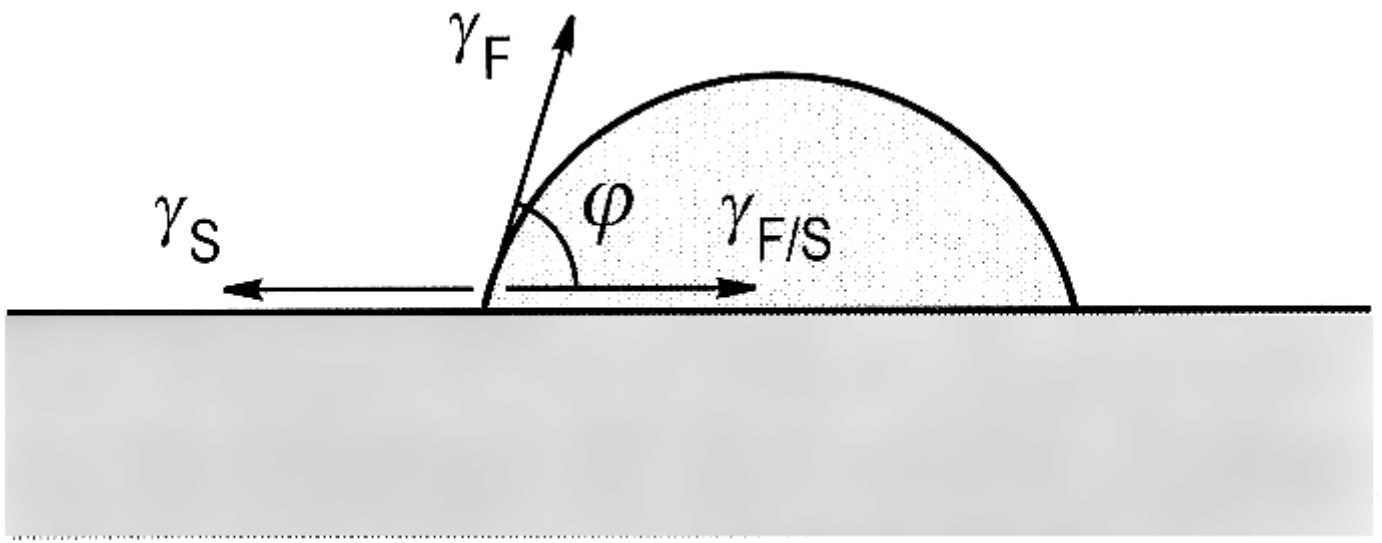

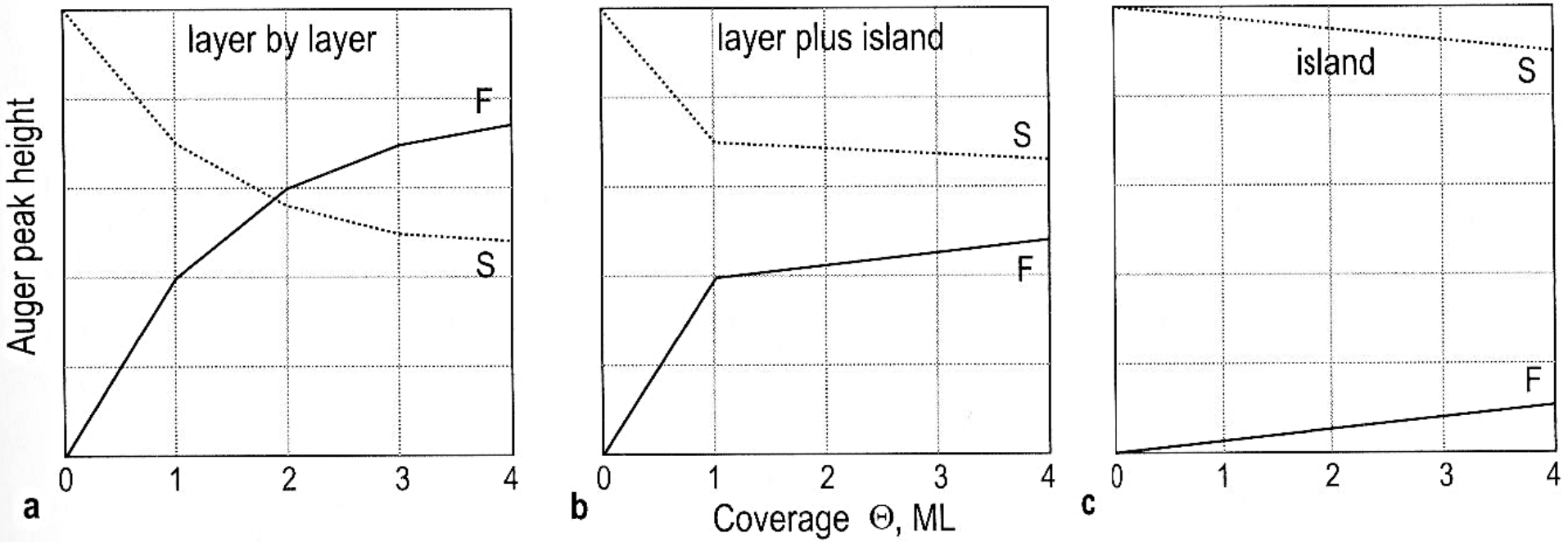

Fig. 14.3. Schematic plot of the Auger amplitude fron the film (F) and substrate (S) versus the amount of deposited material for thre main growth modes: (**a**) layer-by-layer (FM) growth; (**b**) layer-plus-island (SK) growth; and (**c**) island (VW) growth

Nukleation & Wachstum: Basisprozesse

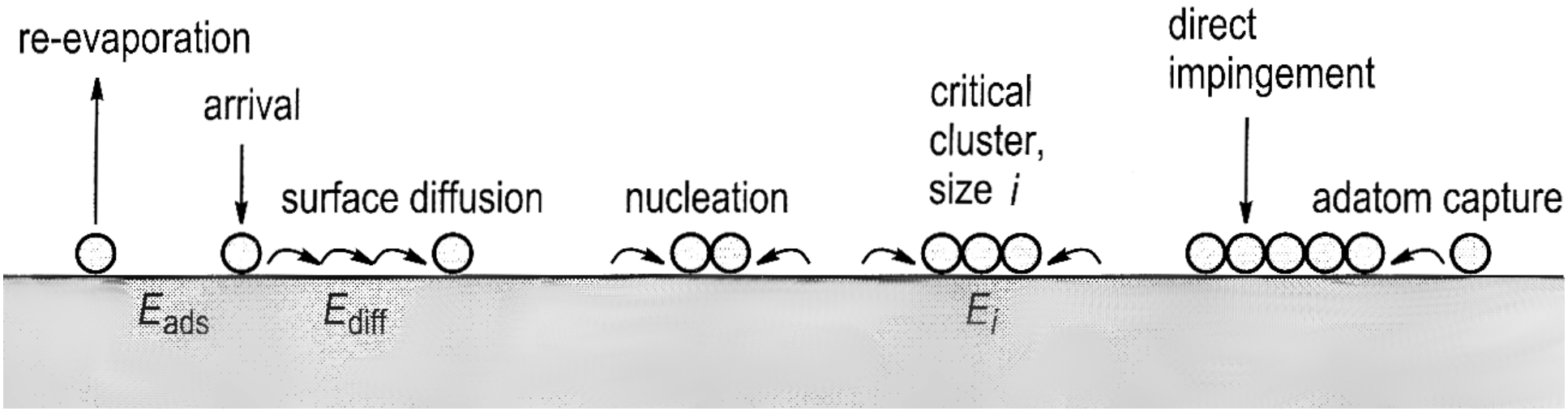

Flüsse zwischen Clustern

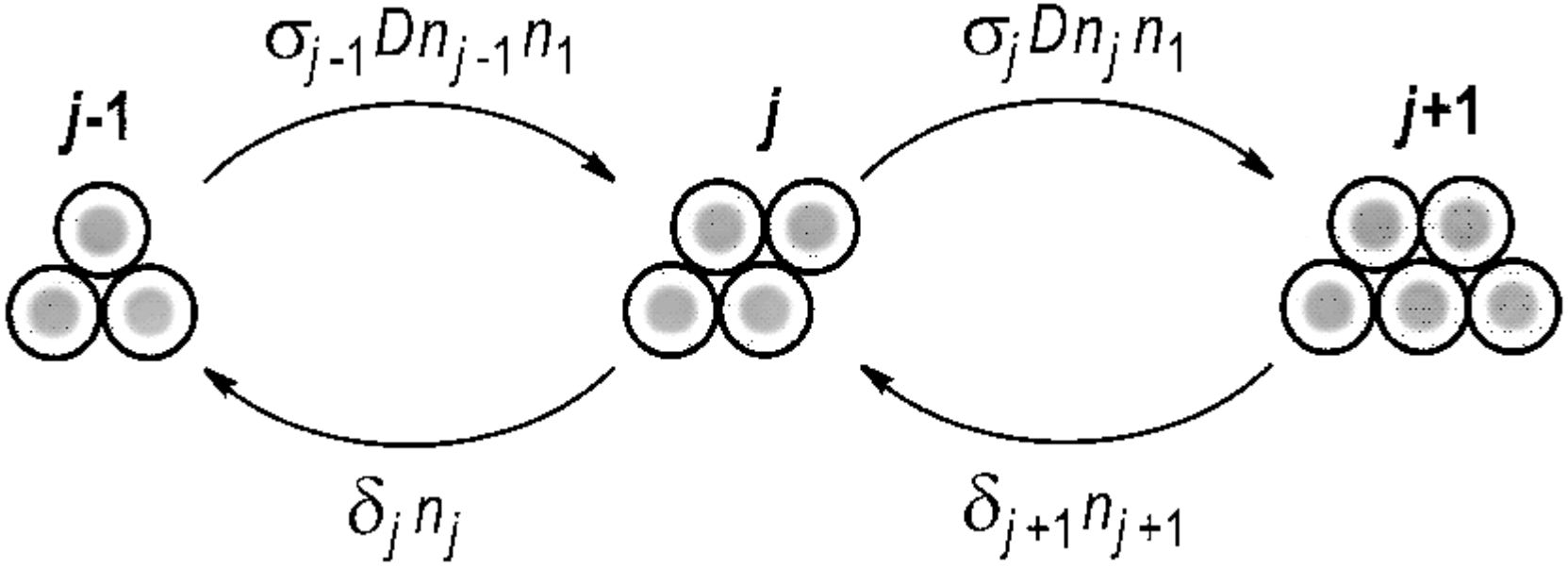

Numerische Lösung der Ratengleichungen

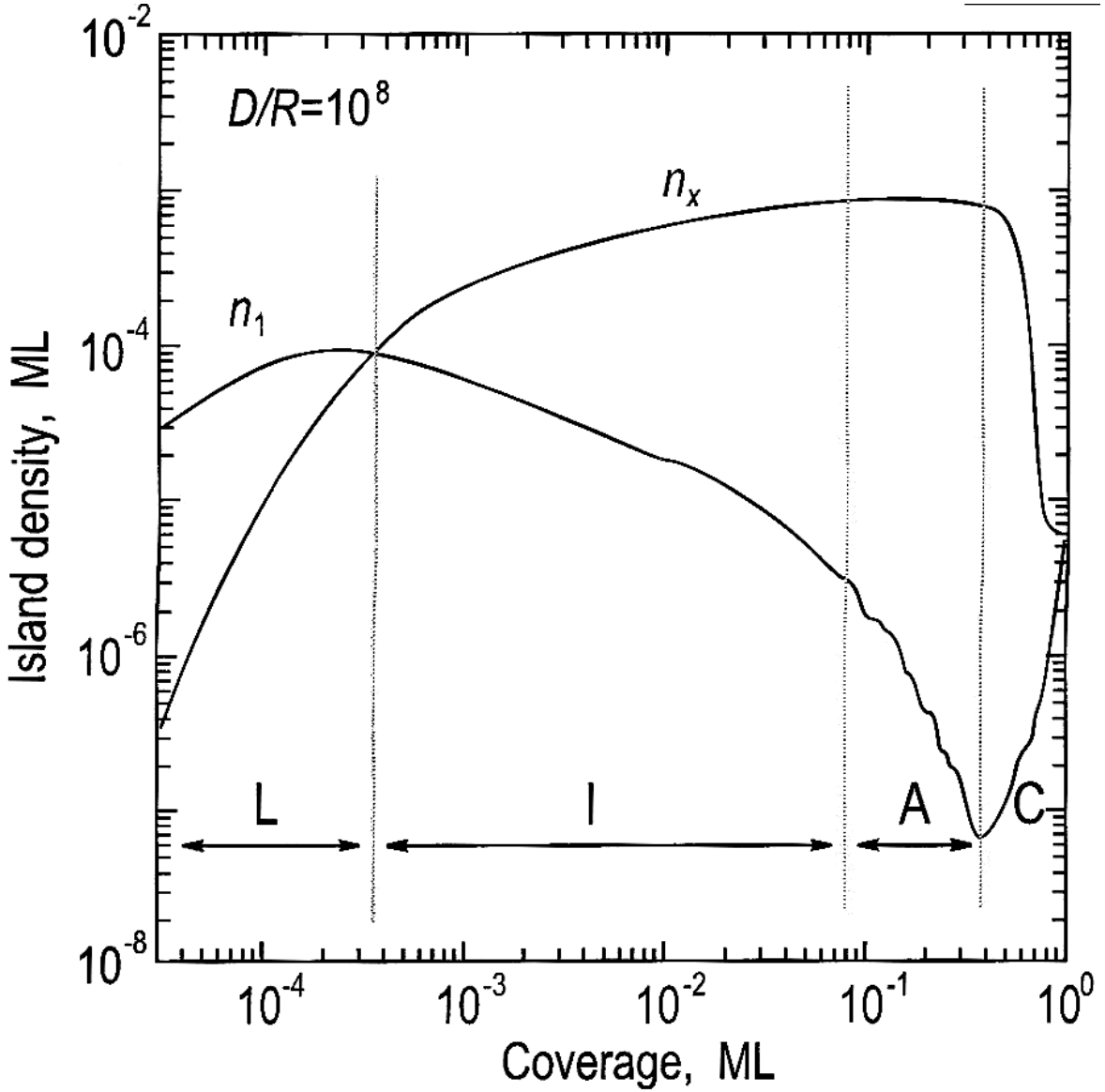

Fig. 14.6. Number density of adatoms (n_1) and islands (n_x) versus coverage in the case $i = 1$ and $D/R = 10^8$, showing four regimes: a low-coverage nucleation regime (L); an intermediate-coverage regime (I); aggregation regime (A); and a coalescence and percolation regime (C) (after Amar, Family and Lam [14.1])

Diffusion Limited Aggregation

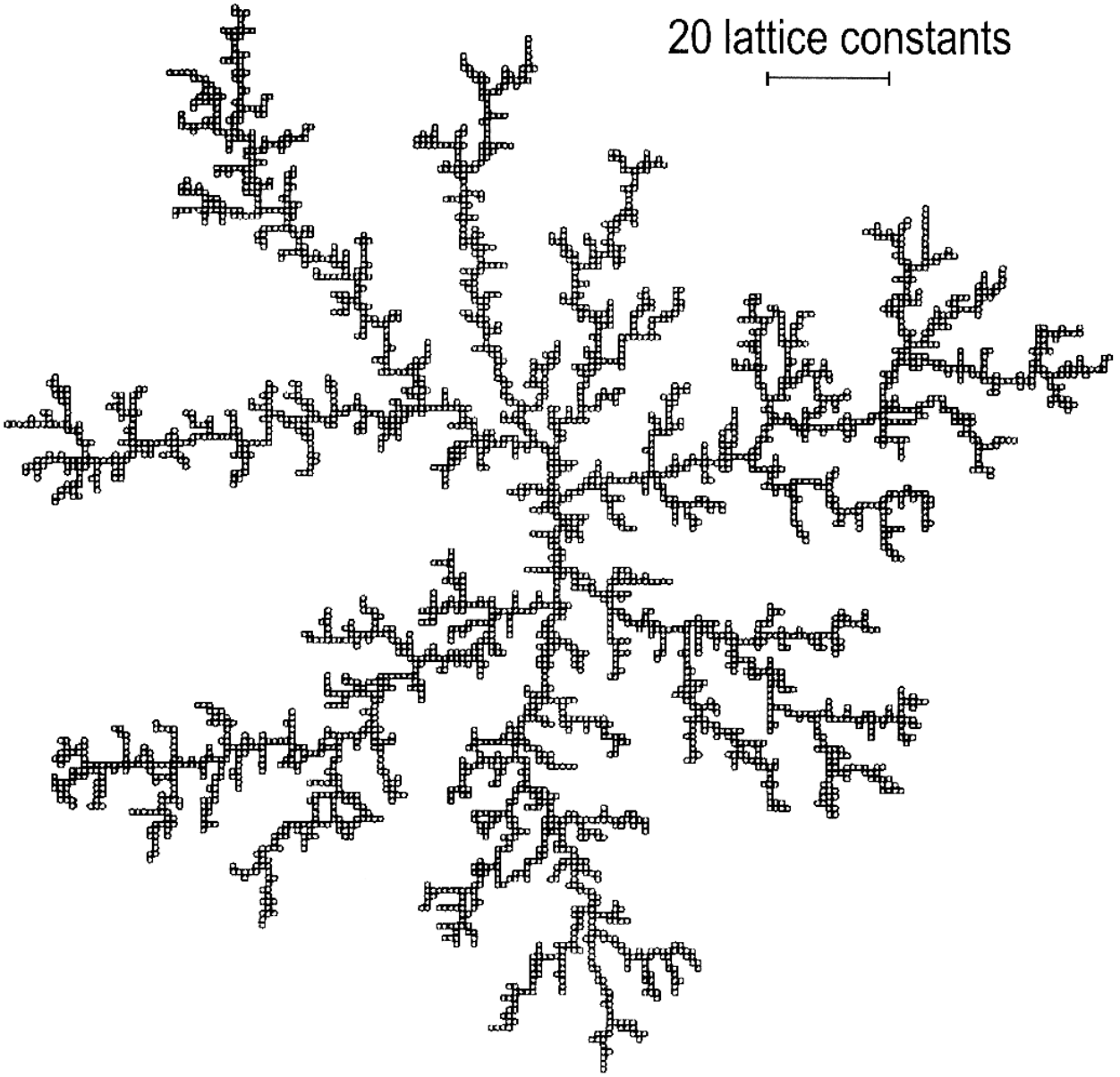

Fig. 14.9. Classical DLA aggregate of 3600 particles on a square lattice (after Witten and Sander [14.4])

Pt/Pt(111): Inselform

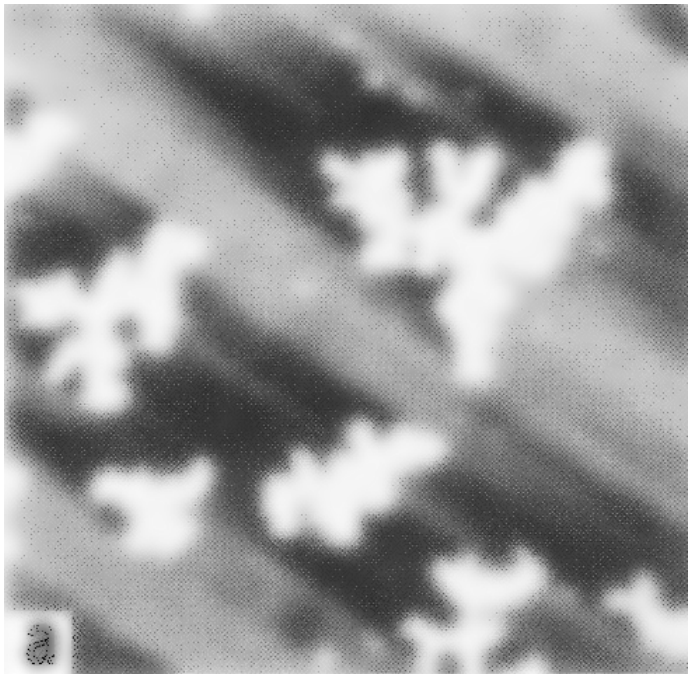

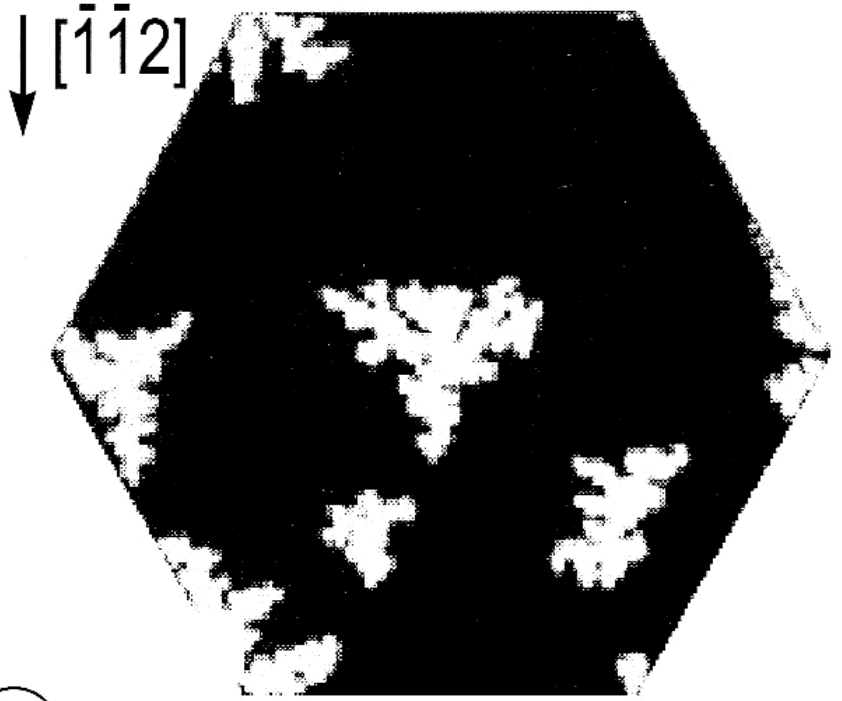

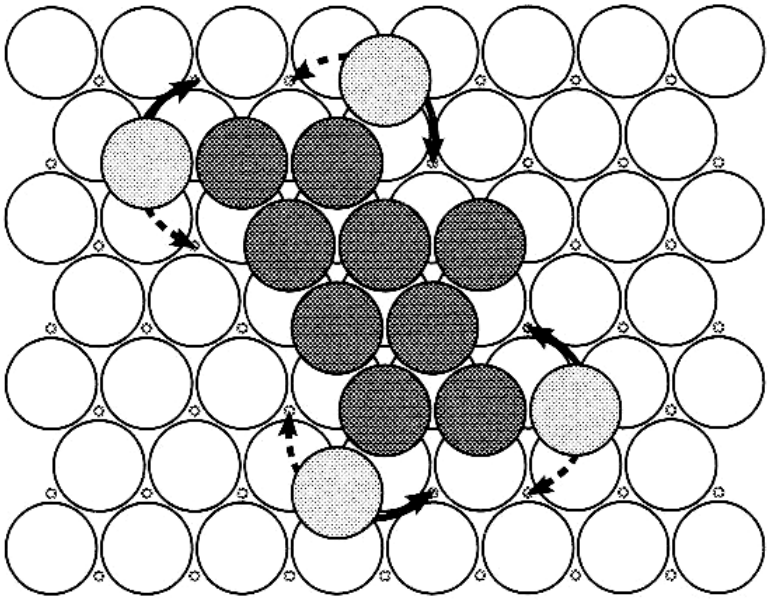

Fig. 14.10. (**a**) Experimental (500×500 Å^2 STM image) and (**b**) simulated island shapes in the Pt/Pt(111) system at 245 K. (**c**) Ball model illustrating the mechanism of anisotropic island growth. The lightly shaded atoms at the corners are onefold coordinated. Dashed and full arrows indicate diffusional jumps into twofold coordinated sites via atop positions (non-preferential path) and via bridge positions (preferential path), respectively (after Hohage et al. [14.5])

Pt/Pt(111) – Inselform: Temperatureinfluss

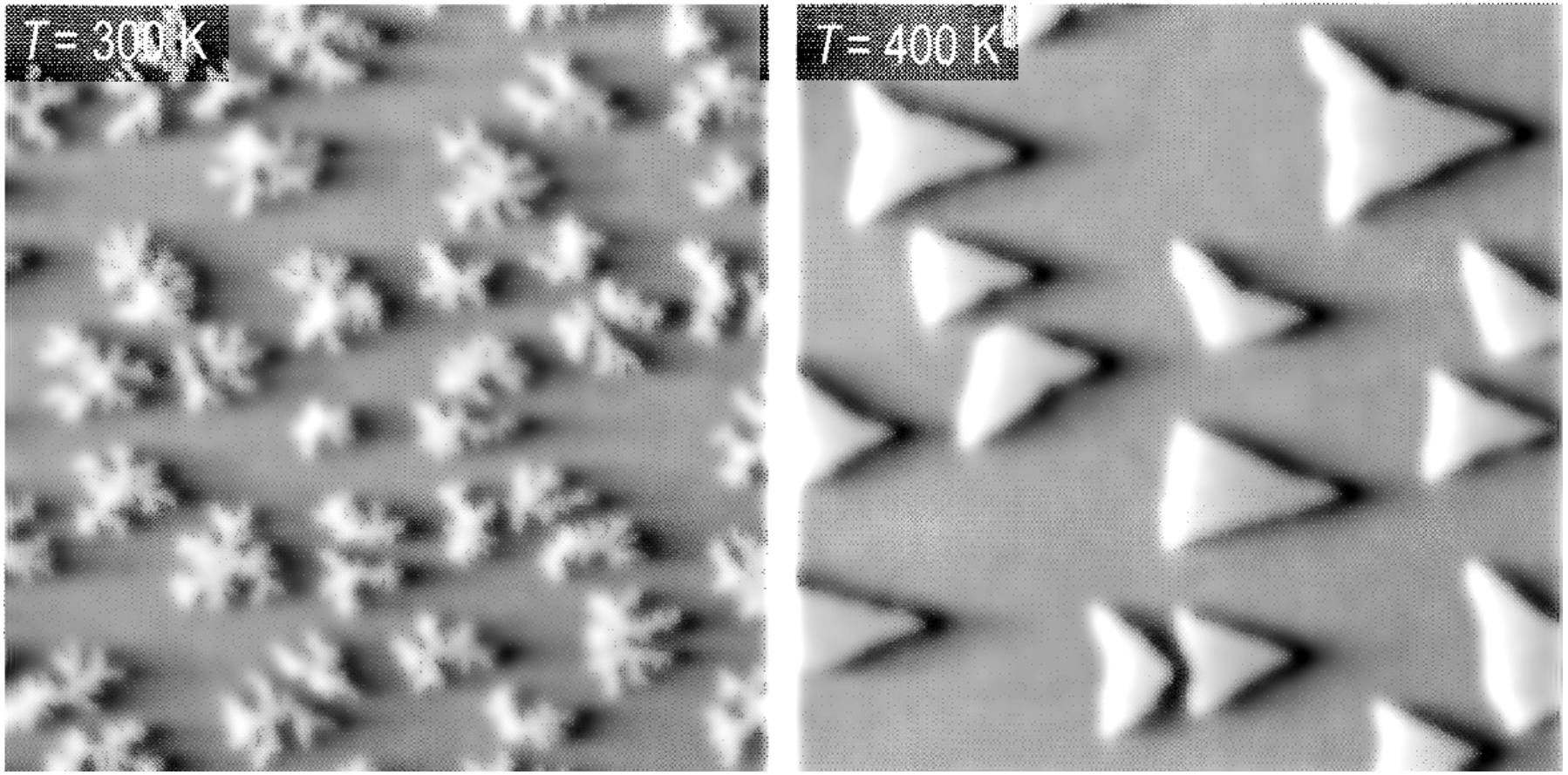

Fig. 14.11. Effect of growth temperature on island shapes in the homoepitaxial growth of Pt on Pt(111). (**a**) Growth at 300 K results in the formation of ramified islands. (**b**) At 400 K compact islands of triangular shape are formed (after Bott et al. [14.6])

Pt/Pt(111): *Gleichgewichts*inselform

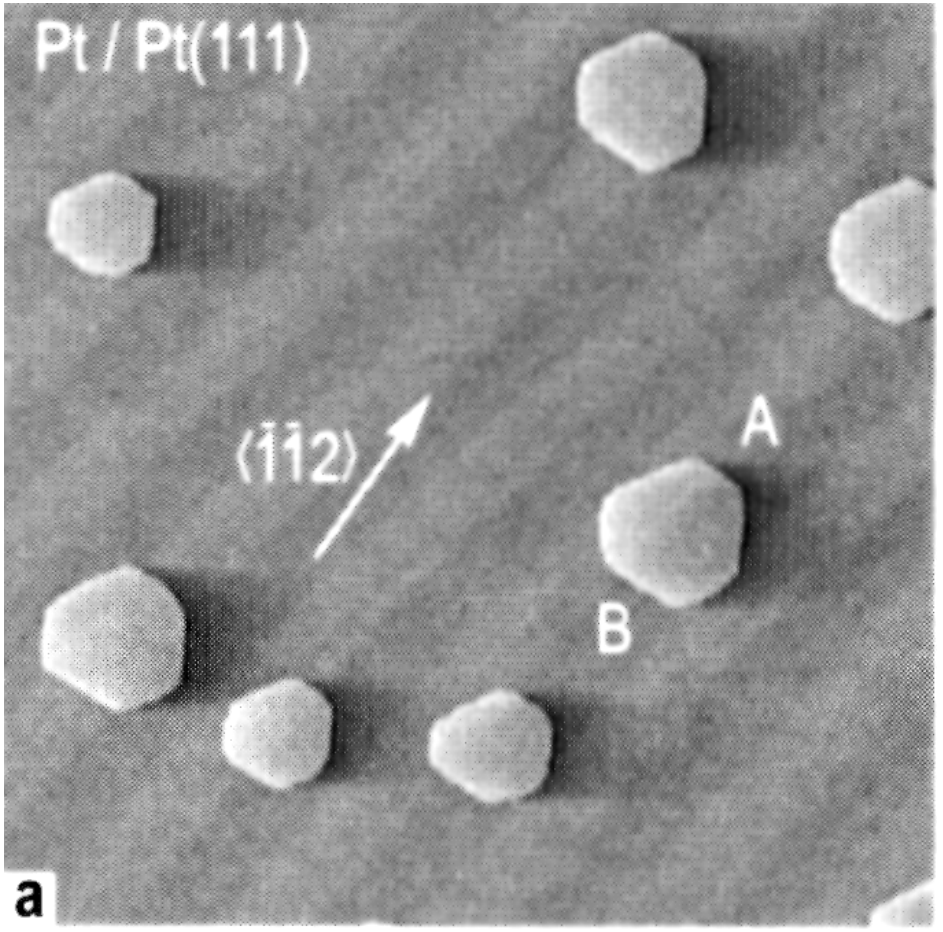

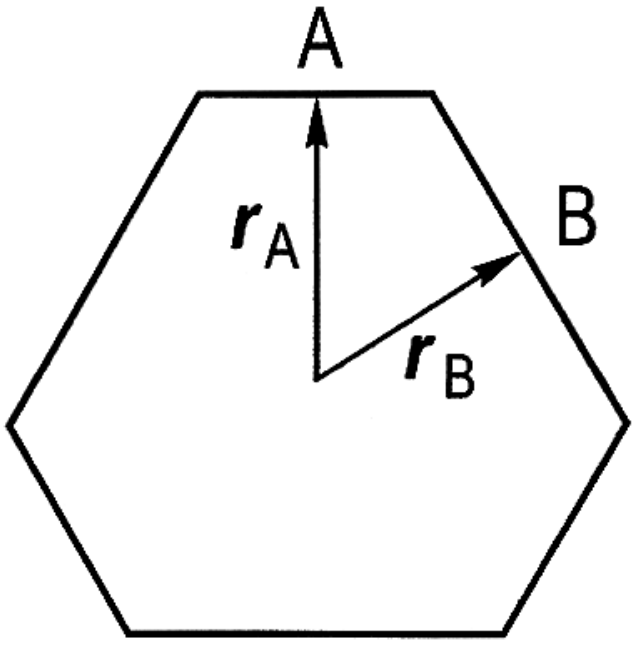

$$\frac{|r_B|}{|r_A|} = \frac{\gamma_B}{\gamma_A} = 0.87 \pm 0.02$$

Fig. 14.12. (**a**) 2000×2000 Å^2 STM image of monatomic Pt islands on Pt(111) formed by deposition of 0.1 ML at 425 K followed by annealing to 700 K for 60 s. The islands reveal their equilibrium shape with A-step segments being considerably smaller than B-step segments (measured length ratio 0.66±0.05). (**b**) Schematic diagram illustrating the application of the 2D Wulff theorem for the determination of the ratio of the step free energies. For Pt(111) the ratio of the free energies of the B-step and A-step is found to be 0.87±0.02 [14.7] (after Michely [14.8])

Koaleszenz: Inseln auf Ag(111)

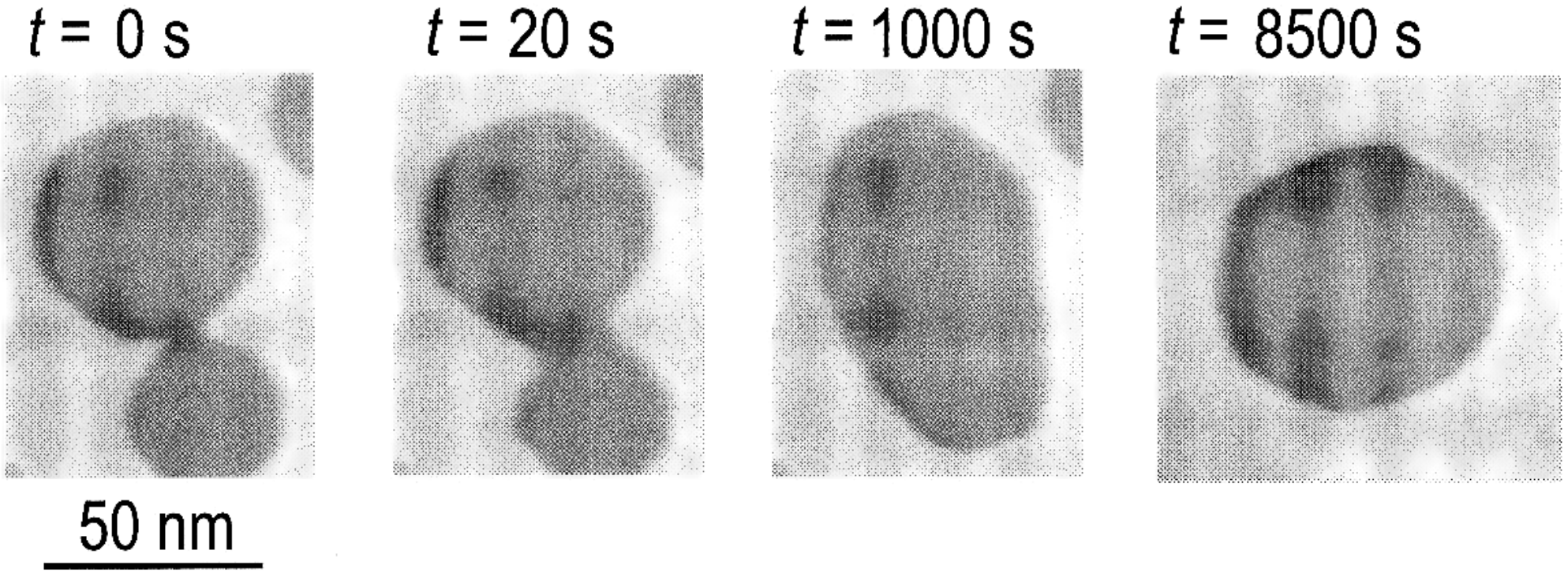

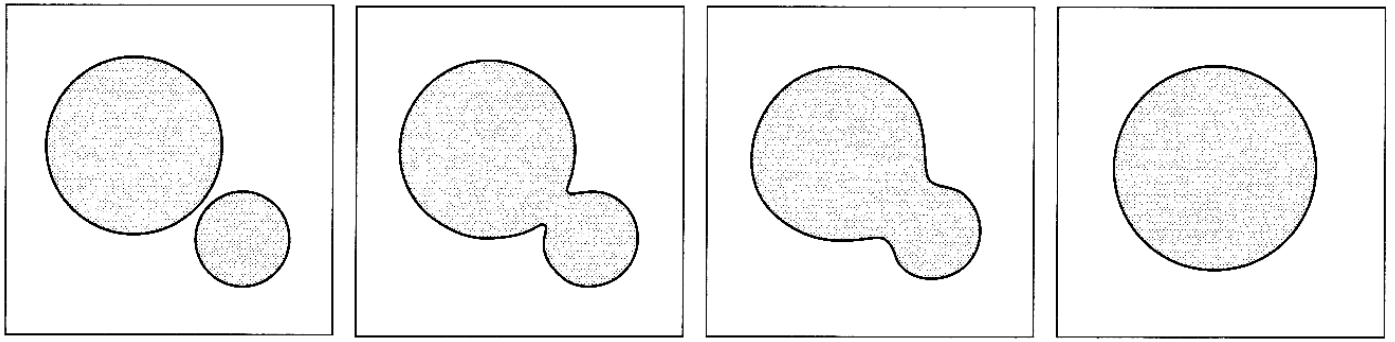

Ostwaldreifen

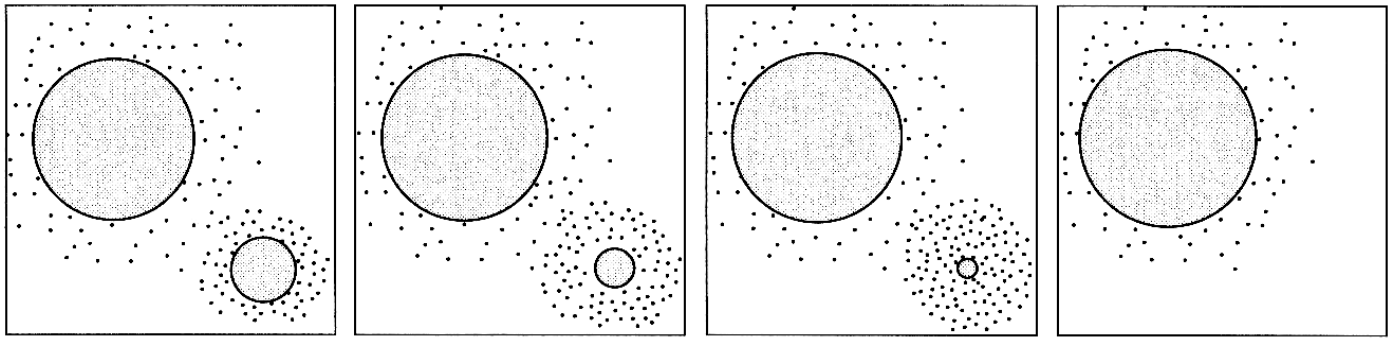

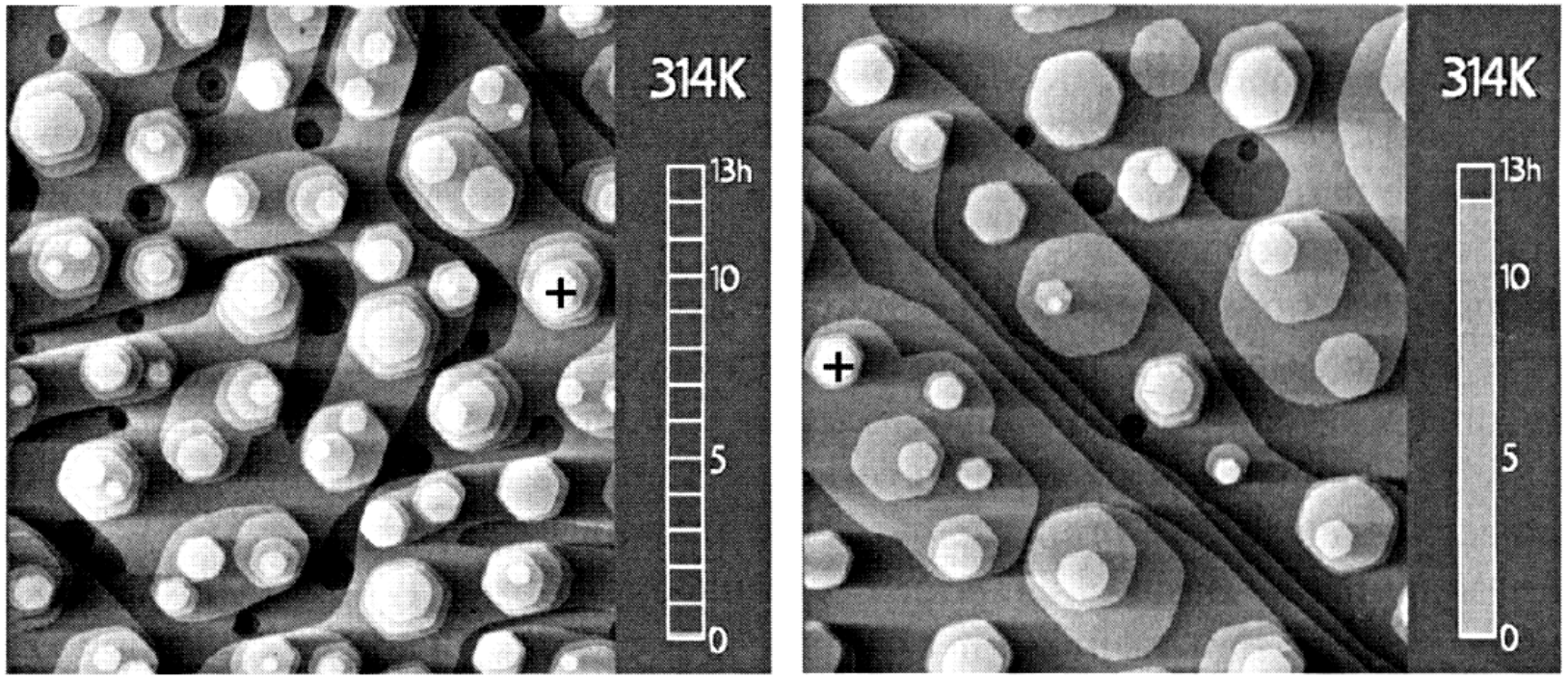

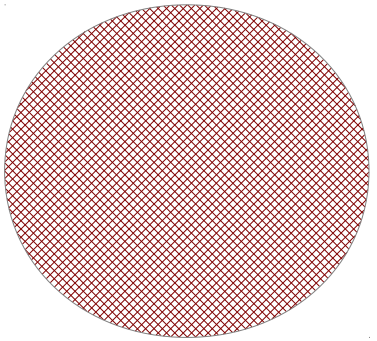

Fig. 4.1. STM image of a Cu(111) surface (left) shortly after deposition of several monolayers of Cu and (right) after 12 h (courtesy of Margret Giesen). Each contrast level corresponds to one monolayer. The black cross marks the same spot on the surface, which has drifted from left to right. During the time span of 12 h the surface features become larger and the surface flattens. The mean shape of all islands is the same and stays constant during the entire time: the islands are in equilibrium with themselves, while the surface is globally not in equilibrium.

Inter- vs. Intralagentransport: Wachstumsmodi

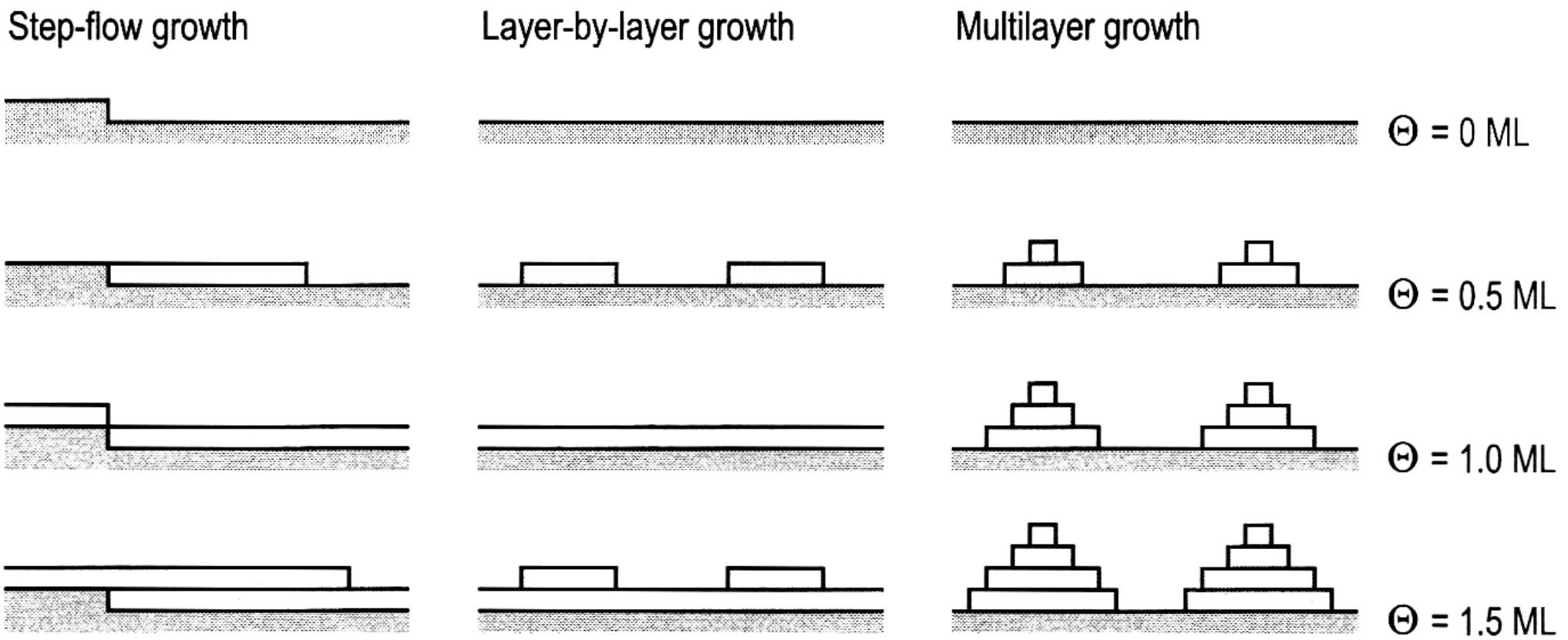

Wachstumsmodi mit Ehrlich-Schwoebl-Barriere

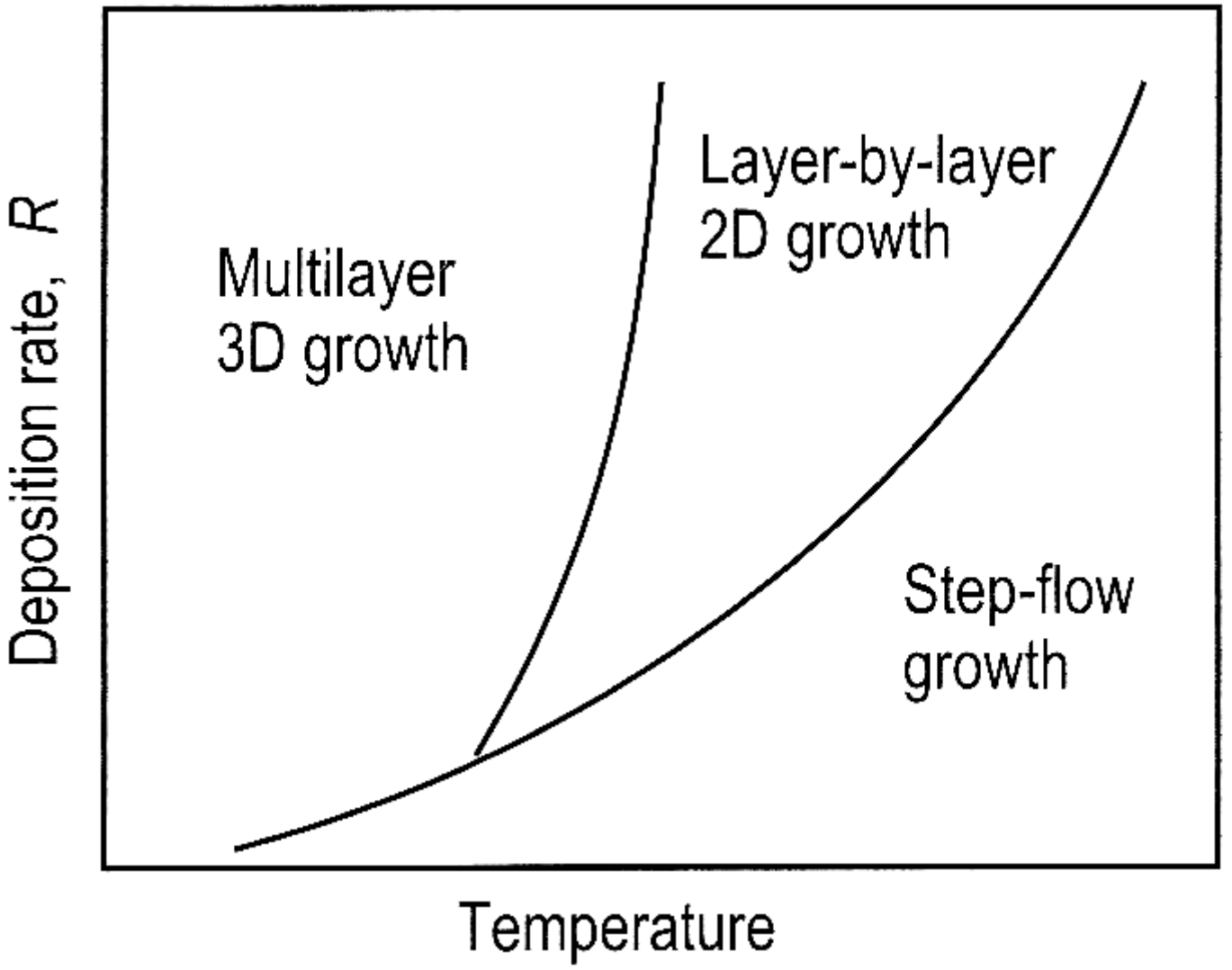

Heteroepitaxie: Wachstummodi

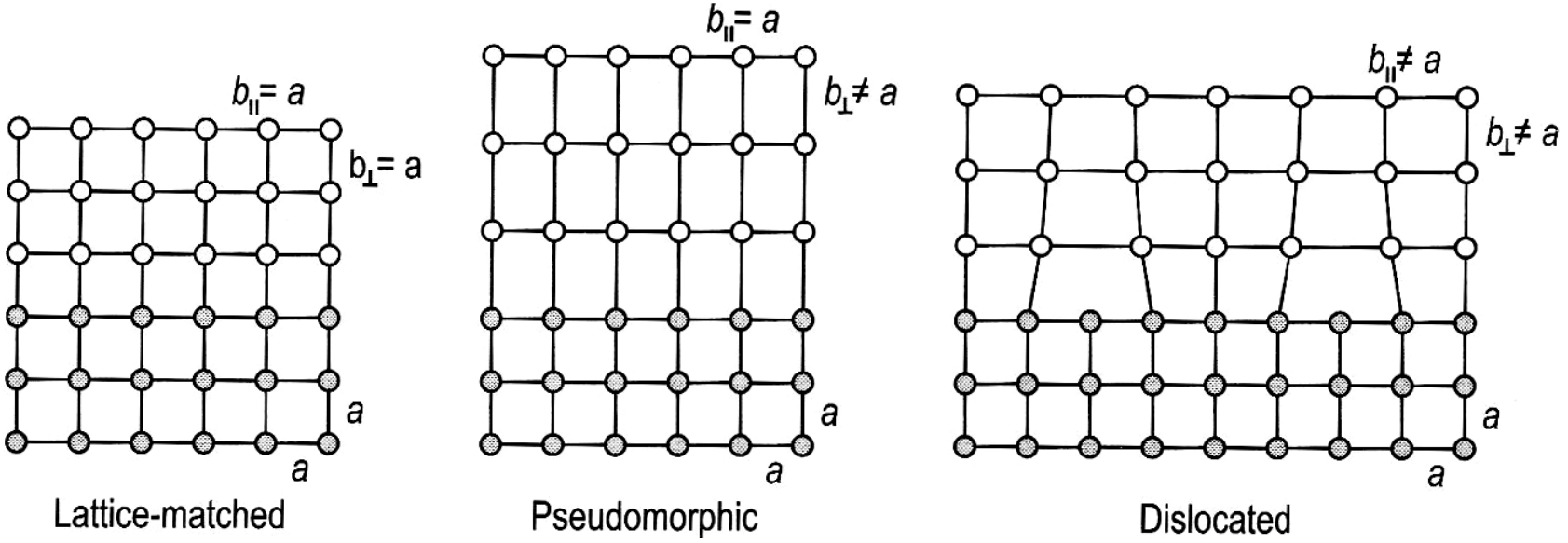

Ce auf Ag(111)

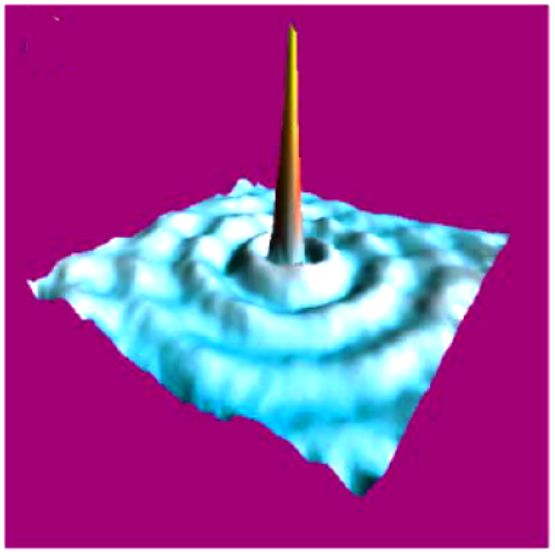

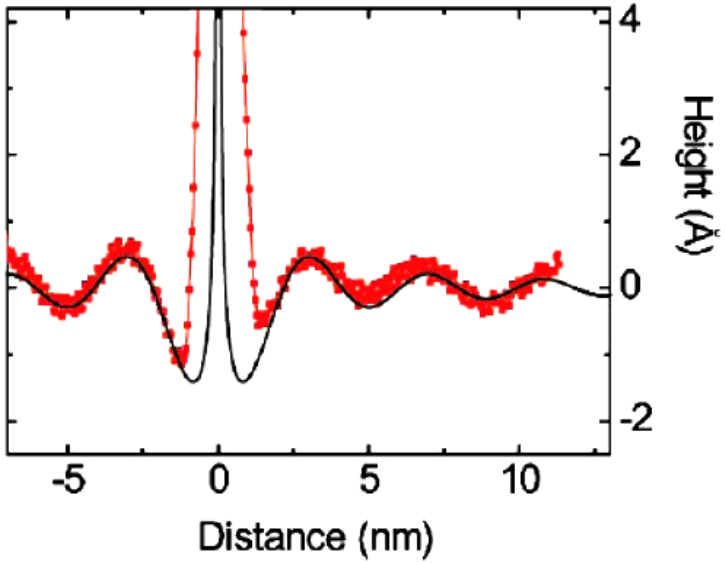

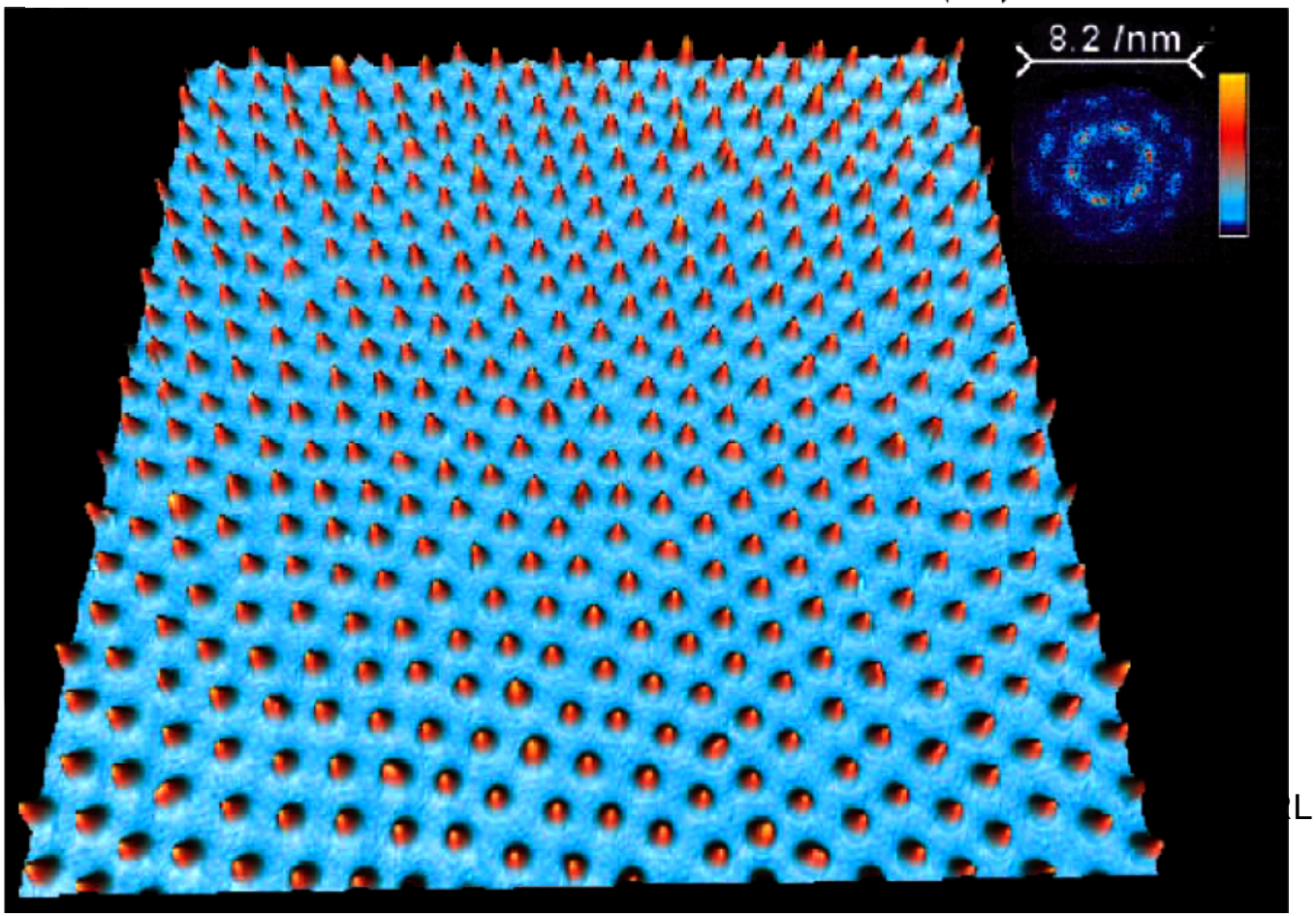

F. Silly et al.,
L **92**, 016101 (2004)

A. Weismann

MNF-phys-1112/1122: Oberflächenphysik III - Nanostrukturen

Do, 10:00 – 11:45 (geplant)

- Graphen
- Elektronenpropagation / Stehwellenmuster / Confinement
- Greensche Funktionen
- Elektronentransport durch Nanostrukturen
- Quantenschrotrauschen
- Spin-Orbit Wechselwirkung

Passing current through touching molecules

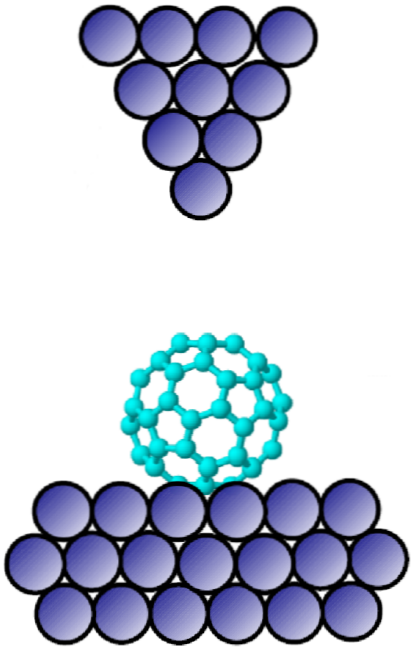

*PRL **98**, 065502 ('07)*

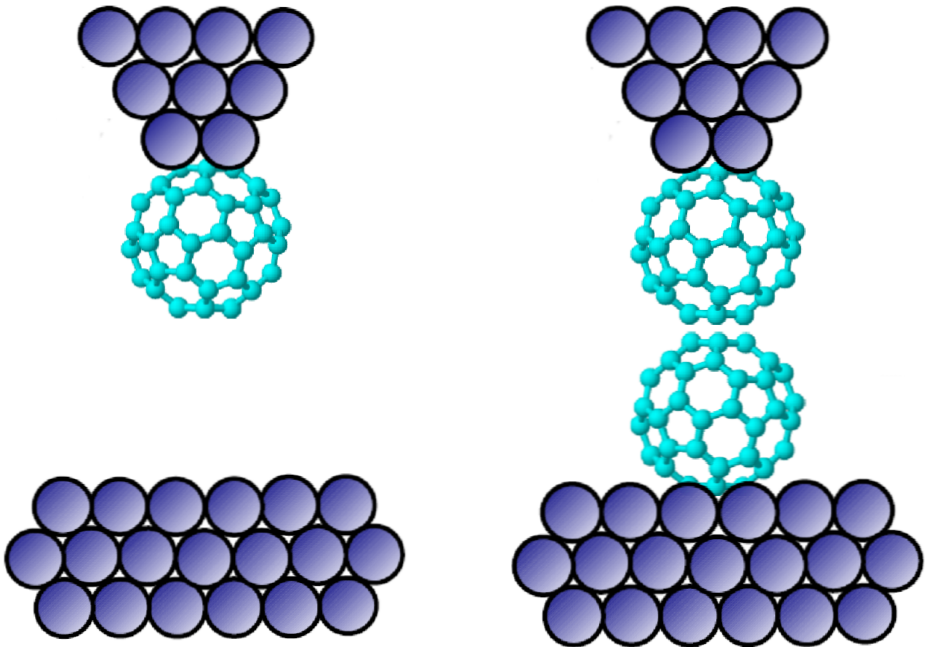

*PRL **103**, 206803 ('09)*